HYDRA: Fabrication of cell culture HYDrogels by Robotic liquid handling Automation for high-throughput drug testing

Eloisa Torchia[1], Moises Di Sante[1], Bohdana Horda[1], Marko Mihajlovic[2], Julius Zimmermann[1], Melissa Pezzotti[1], Elisa Cimetta[3], Sylvain Gabriele[4], Ferdinando Auricchio[5], Johan Ulrik Lind[2], Alessandro Enrico[1,], Francesco Silvio Pasqualini[1,]*.*

1. E. Torchia, M. Di Sante, B. Horda, J. Zimmermann, M. Pezzotti, A. Enrico, F. S. Pasqualini
   Synthetic Physiology Lab, Department of Civil Engineering and Architecture, University of Pavia, 27100, Pavia, Italy
2. M. Mihajlovic, J. U. Lind
   Department of Health Technology, Technical University of Denmark, 2800 Kgs. Lyngby, Denmark
3. E. Cimetta
   Department of Industrial Engineering, University of Padua, 35131 Padova, Italy
4. S. Gabriele
   Mechanobiology & Biomaterials Group, Research Institute for Biosciences, University of Mons, CIRMAP, 20 Place du Parc, Mons B-7000, Belgium
5. F. Auricchio
   Group of Computational Mechanics and Advanced Materials, Department of Civil Engineering and Architecture, University of Pavia, 27100, Pavia, Italy

*Corresponding authors: Email: francesco.pasqualini@unipv.it, alessandro.enrico@unipv.it

Abstract

Traditional plastic- and glass-based cell culture platforms lack physiological relevance which limits their predictive power in drug development. Organoids and organs-on-chip offer biomimicry in late preclinical stages but lack scalability for high-throughput screening (HTS) in earlier stages. In fact, even introducing the simplest critical biomimetic cue, thin hydrogel layers, into the small wells of HTS plates causes the formation of curved menisci that disrupt cell seeding and imaging.

We introduce HYDRA (HYDrogels by Robotic liquid handling Automation), an automated method that enables consistent hydrogel fabrication in HTS plates. We used liquid handling robots to dispense hydrogel precursor solutions and avoid contact with the sidewalls to prevent meniscus formation. We used gelatin for its mild surfactant properties, which allow pinning of the droplet's contact line, promoting uniform spread. Finally, we re-aspirated the excess liquid, leaving behind a hydrogel layer with controlled stiffness and thickness.

We show compatibility with standard 96- and 384-well plates and integration with existing automated workflows, including quality control. We validated HYDRA in dose-response assays using anti-cancer drugs, genetically engineered epithelial cells, phase holography, and fluorescence microscopy. We believe that HYDRA provides a scalable, biomimetic, and therefore more predictive alternative for early-stage screening and in vitro drug testing.

Keywords: fish gelatin, HaCaT Keratinocytes, phase holographic imaging, nocodazole, paclitaxel

1. Introduction

Accurately predicting human cellular responses at preclinical stages is essential for successful drug R&D. Yet, drug discovery programs fail often (90% of the time), slowly (10+ years), and costly (1 BUSD+)[1]. Advances in genomics and artificial intelligence have accelerated early-stage discoveries[2,3], but productivity continues to decline, and clinical attrition rates remain high[4,5]: ~50% of compounds that pass initial preclinical assays still fail in subsequent human trials, reflecting the poor predictive capacity of traditional preclinical models[1,6]. This is perhaps not surprising since cell-based assays – especially the early automated high-throughput screening (HTS) - have predominantly relied on rigid substrates such as plastic and glass, which distort tissue architecture, alter mechanical and metabolic signaling, and impair interactions between cells and the extracellular matrix (ECM), compromising assay relevance[7].

The effect of improved biomimicry on predictivity has been demonstrated by the success of engineered culture systems that replicate the native tissue microenvironment more closely than standard cell culture formats[8]. However, these systems haven't reached the throughput necessary to effectively be employed in early HTS. Spheroids and organoids both provide three-dimensional cell–cell and cell–ECM interactions, accurately recapitulating tissue architecture and clinically relevant disease phenotypes[9]. Their potential compatibility with multiwell plates also makes them attractive candidates for HTS[10,11]. However, their size, stochastic structural organization, and inherent optical scattering significantly limit quantitative high-resolution microscopy, complicating routine use in imaging-based HTS[8]. Moreover, organoids typically lack integrated vasculature, necessitating additional complex microfluidic engineering[12–14]. Organs-on-chip similarly capture complex tissue functionality through precise control of mechanical and biochemical conditions within microfluidic platforms[9]. Their planar configuration facilitates high-resolution microscopy and optical clarity. Yet, the intricate and custom nature of microfabrication currently prevents scalable production, severely restricting their practical implementation within automated, high-throughput pipelines[8].

Planar hydrogel substrates could provide an advantageous balance between physiological relevance, imaging clarity, and HTS scalability. Hydrogels are widely utilized in organoids and chips, as they offer adjustable biochemical composition, substrate stiffness, and optical transparency[15–17], essential for accurate mechanobiology studies[18]. Yet, casting uniform, thin hydrogel layers within multiwell HTS plates remains technically challenging: capillary forces at the small-diameter well edges induce curved

menisci, disrupting cell attachment, uniform growth, and high-resolution microscopy[19]. Recent efforts sought to overcome these limitations. Brooks et al. formed PEG-based hydrogels in 96-well plates through photocrosslinking, yielding tunable stiffness, yet the thick (500–1000 µm) gels compromised optical resolution[20]. At the other end of the spectrum, Machillot et al. utilized a layer-by-layer coating to create single micron hydrogel layers[21], but these coatings were insufficiently thick to shield cells from the underlying stiff plastic substrate, influencing cellular responses[22].

Here, we introduce HYDRA (HYDrogels by Robotic liquid-handling Automation) a scalable and automated solution to generate uniform, micrometric planar hydrogels directly within standard HTS plates. HYDRA works by robotically dispensing a sub-contact volume of hydrogel precursor solution, carefully preventing it from contacting well sidewalls. Immediate controlled re-aspiration pins the solution's contact line through contact angle hysteresis, yielding a thin, uniform precursor layer. Enzymatic crosslinking of this residual layer produces flat hydrogel films of 10–50 µm thickness (Fig. 1a–b). By selecting cold fish gelatin, which remains liquid at room temperature, we ensure process compatibility with existing automated liquid-handling workflows[23]. We validated this approach using engineered fluorescent HaCaT epithelial cells cultured in both 96- and 384-well plates (Fig. 1c–e), demonstrating robust adherence, normal proliferation, and suitability for high-resolution, imaging-based drug-response assays[24].

Thus, HYDRA leverages established HTS automation and microscopy infrastructure, delivering physiologically relevant, easily implementable substrates to pharmaceutical screening programs without new capital investments.

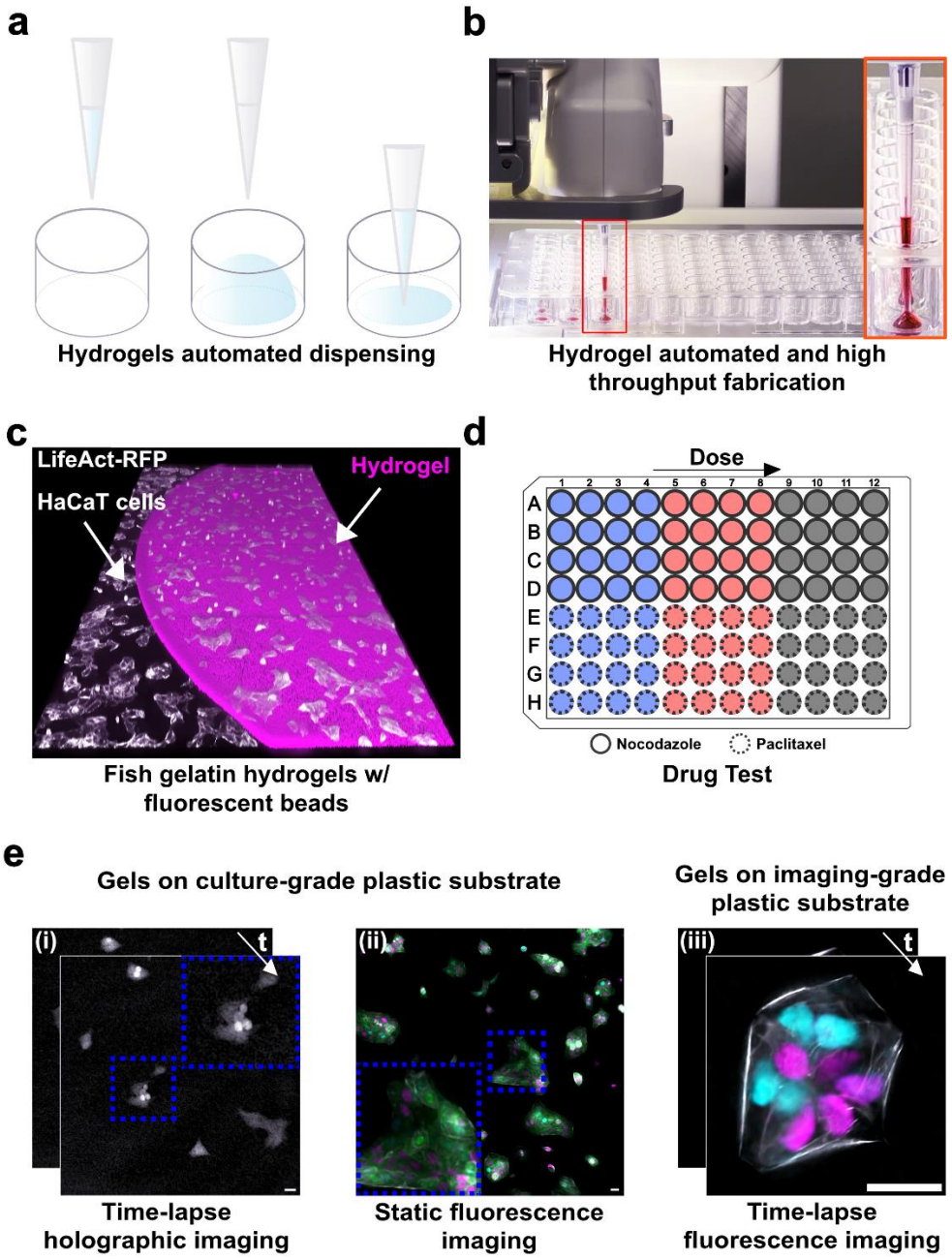

Fig. 1. HYdrogel Dispensing method with Robotic Automation (HYDRA) for HTS-compatible hydrogels. (**a**) Schematic illustration of the Hydrogel Dispensing with Robotic Automation (HYDRA) method. (**b**) Photograph of the robot performing the HYDRA of fish gelatin (FG) hydrogels in a 96-well plate. A red food colorant was added for visualization purposes. (**c**) Isometric confocal z-stack (3D rendering) of an enzymatically crosslinked FG hydrogel embedding fluorescent beads and HaCaT cells seeded on top and on the side of the hydrogel. (**d**) Schematic representation of drug tests performed with nocodazole and paclitaxel. Drug dose (three concentrations of each drug color-coded as blue – low concentration, red – medium concentration, and black – high concentration) increases along columns. (**e**) Gel compatibility with standard imaging approaches in high throughput plates using HaCaT cells. (i) Time-lapse holographic imaging for long-term low phototoxicity studies and (ii) static fluorescence imaging of cells treated with nocodazole or paclitaxel drugs and imaged for 48 hours after treatment. In both cases the gels were cast on inexpensive traditional tissue culture plastic. iii) High-resolution fluorescence imaging experiments of HaCaT cell proliferation for 18 hours (high magnification, 40x silicon oil objective). The white, green, cyan, and magenta colors in (ii) and (iii) correspond to actin, tubulin, and nuclei of cells in the G1 and S/G2 phases, respectively. Scale bars: 25 μm.

3. Results

3.1 Rheological studies of fish gelatin hydrogels

To implement HYDRA within automated HTS pipelines, we first needed to verify that fish gelatin (FG) hydrogels meet essential mechanical and dispensing requirements. We cross-linked FG chemically using TG to fabricate hydrogel-based cell culture platforms with HYDRA (Fig. 2a)[25,26]. Critically, we selected FG because aqueous solutions of FG remain liquid at room temperature (RT) and must be cooled to 4 °C to form a physical gel. The viscosity of FG should thus stay low and stable at RT to make dispensing possible[27]. We first used oscillatory rheometry to optimize hydrogel casting in 96-well plates and to verify FG's compatibility with robotic dispensing by quantifying its viscosity at RT. The viscosity at zero shear rate measures the material's viscosity at rest, and we observed this measure doubling in our precursor solution when we doubled (from 0.67 ± 0.18 to 2.11 ± 0.06 Pa·s) the FG concentration, in good agreement with the literature (Fig. 2b)[26,28]. Still, unlike gelatin solutions obtained from mammalian sources, it remained below the threshold for pipettability with air displacement pipettes[29–31].

The gelation point of the FG hydrogels is expected to decrease with higher polymer concentration[26]. To test FG pipettability across a more extensive range of conditions, we examined FG physical gelation using the tube inversion method. Specifically, we prepared three FG concentrations (5% w/v, 10% w/v, and 20% w/v in PBS -/-) to generate gels with physiological stiffness when mixed with TG[28]. We dispensed FG solutions into microcentrifuge tubes, placed them at RT and 4 °C for 72 hours, and took pictures after 24 hours upon inversion (Supplementary Fig. S1). All the mixtures flowed with gravity except for the 20% FG mixture at 4 °C, for which viscosity was high enough to counter the gravitation pull, Furthermore, we analyzed chemical gelation by crosslinking gelatin solutions with 2% w/v TG at RT and 4 °C for 72 h. Independent of temperature and concentration, all FG solutions formed gels within

72 h (Fig. S1)[26]. These results show that, in principle, a liquid-handling robot can dispense FG solutions at room temperature.

To ensure gelation occurred only after completing automated dispensing across the entire plate, we evaluated gelation onset using previously reported TG concentrations optimized for bioprinting (0.5% and 2% w/v)[32]. Both TG concentrations resulted in a gradual crosslinking process (Fig. 2c-d). Specifically, the storage modulus (G') and loss modulus (G') curves associated with 0.5% w/v TG suggested that crosslinking proceeded more slowly at this concentration (Fig. 2c). In comparison, the curves for 2% w/v TG reached a plateau at approximately 3 h after mixing (Fig. 2d). For 10% w/v FG hydrogels crosslinked with 2% w/v TG, the crossover point was reached after approximately 40 min, suggesting that rapid blending of the two components in an HTS plate format should not trigger partial gel formation.

Finally, we evaluated whether the selected concentrations yielded substrates with stiffness within the physiological range by measuring the shear modulus of the hydrogels. (Fig. 2e-f). Samples crosslinked with 2% w/v TG exhibited G' ranging from 500 Pa to 3 kPa (Fig. 2e and Supplementary Fig. S2), again in good agreement with the literature[26]. Finally, to understand the effect of TG on the resulting hydrogel stiffness, we used a gelatin concentration of 10% w/v and varied TG concentrations from 0.5% to 2% w/v (Fig. 2f, Supplementary Fig. S2c-d, and S3). We found that the value of G' increased (from 500 Pa to approximately 2 kPa) with increasing TG concentration (Fig. 2f and Supplementary Fig. S3). This trend and the G' values align with previous works reporting on fish gelatin hydrogels chemically crosslinked at 37 °C[33]. Together, these results demonstrated the viscosity of fish gelatin at room temperature can be managed using a liquid handling system, even with high protein concentrations (20% w/v). We also found that the dispensed hydrogels displayed physiologically relevant stiffness when cross-linked with TG.

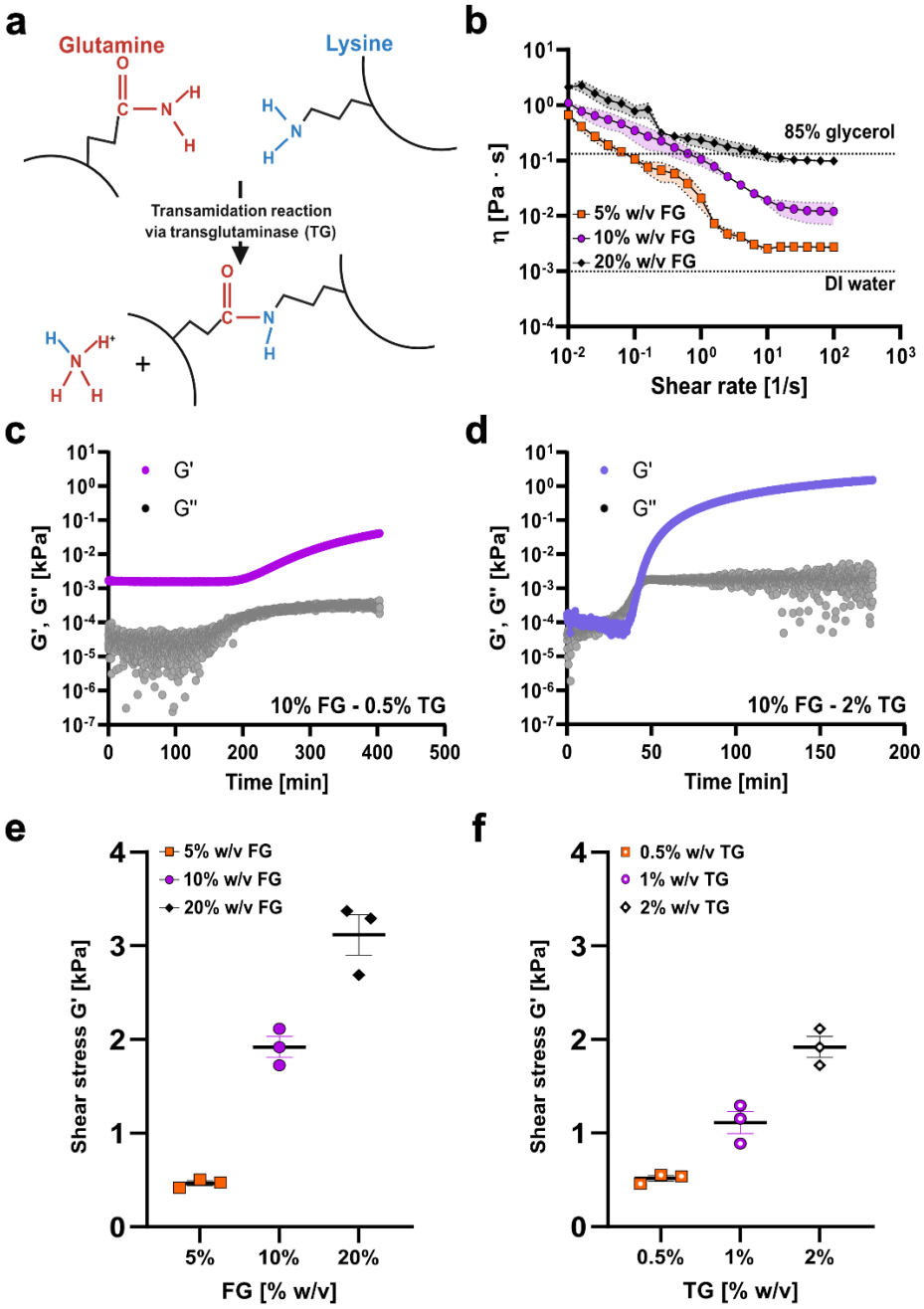

Fig. 2. Rheology of fish gelatin hydrogels. (**a**) Schematic of FG hydrogels chemically crosslinked with TG. Glutamine residues in proteins can form covalent bonds with lysine residues through a transamidation reaction, which produces ammonia as a byproduct, which is washed away during the rinsing steps. In this process, the γ-carboxamide groups of glutamines serve as acyl donors, while the ε-amino groups of lysine function as acyl acceptors. Created with Biorender.com. (**b**) Viscosity vs. shear rate for three different concentrations of FG alone (5% - orange squares, 10% - purple dots, and 20% w/v - black diamonds). Dashed lines stand for viscosity values of 85% glycerol and deionized water at room temperature. (**c**) G' and G'' vs. time for FG at 10% w/v concentration crosslinked with 0.5% w/v TG. (**d**) G' and G'' vs. time for FG at 10% w/v concentration, cross-linked with 2% w/v of TG. Data are displayed as mean ± s.e.m (n=3 samples). (**e**) Shear modulus G' vs. FG concentration (5% - orange squares, 10% - purple dots, and 20% w/v - black diamonds). FG solutions were crosslinked with 2% w/v TG. Data are displayed as mean ± s.e.m (n=3 samples). (**f**) Shear modulus G' vs. TG concentration (0.5% - orange squares, 1% - purple dots, and 2% w/v - black diamonds). 10% w/v fixed FG was used. Data are displayed as mean ± s.e.m (n=3 samples).

3.2 Modelling, fabrication, and characterization of hydrogel thin film in 96-well plates

To optimize hydrogel fabrication by minimizing meniscus formation and maximizing substrate coverage, we used finite-element modeling (FEM) in COMSOL. First, we simulated a classical meniscus formation scenario in which the dispensed volume caused wetting of the sidewalls (Fig. 3a; Supplementary Movie S1). Then, we computed the ratio between the radius of the hydrogels with the air-liquid interface parallel (± 3°) to the substrate and the radius of the well. This configuration led to the gel covering the entire area of the well (100% radial coverage), but the high curvature meniscus severely limited the available planar area (10% flatness). Next, we reduced the dispensed volume to avoid wall contact and applied a receding-angle correction to simulate contact-line pinning during re-aspiration (Supplementary Movie S2)[34]. To identify the optimal dispensing volume, we tested four volumes (6, 12, 18, and 24 µL). Without wall contact, both gel coverage and flatness improved with larger volumes, peaking at 18 µL. At 24 µL, however, wall wetting reduced flatness substantially. To account for the fabrication non-idealities, we also introduced small fluctuations in the simulation parameters: ±20% on dispensed volume; -100 µm and -200 µm on the well radius because of the fabrication tolerance of the well plate and the accuracy of the robot. Considering these fluctuations, we verified that dispensing 18 µL may result in wall wetting (Supplementary Fig. S4). Therefore, we selected 12 µL for the experiments in this study, which reduced coverage by ~20% and increased flatness by 4.5 times concerning the meniscus-inducing conditions (Fig. 3 b and Supplementary Fig. S4).

Accordingly, we automated FG hydrogel fabrication in 96-well plates using an Integra liquid-handling robot, dispensing and immediately re-aspirating 12 µL of precursor solution (visualized using red colorant) to leave only a thin boundary layer. This procedure required about 10 minutes, well within the 40-minute gelation threshold established earlier (Fig. 3c; Supplementary Movies S3 and S4).

Next, To verify compatibility with standard microscopy, we characterized hydrogel thickness and flatness by embedding fluorescent beads within the gels and seeding epithelial cells expressing a red fluorescent actin marker (Life Act™) (Fig. 3d). Using a 20X air objective (NA 0.75), we captured two images, one at the top of the gel and the other at the bottom of the well, by focusing on cell actin and the fluorescent beads. The samples exhibited an expected dose-dependent increase in thickness, from ~10 µm to ~30 µm, and inter-group reproducibility (Fig. 3e and Supplementary Fig. S5). This result agrees with the literature, which sets the cut-off point for how deeply cells sense substrates at 10-20 µm[22]. Together, these results support the idea that liquid handling automation can reproducibly form thin hydrogel layers for cell culture in commercial HTS plates.

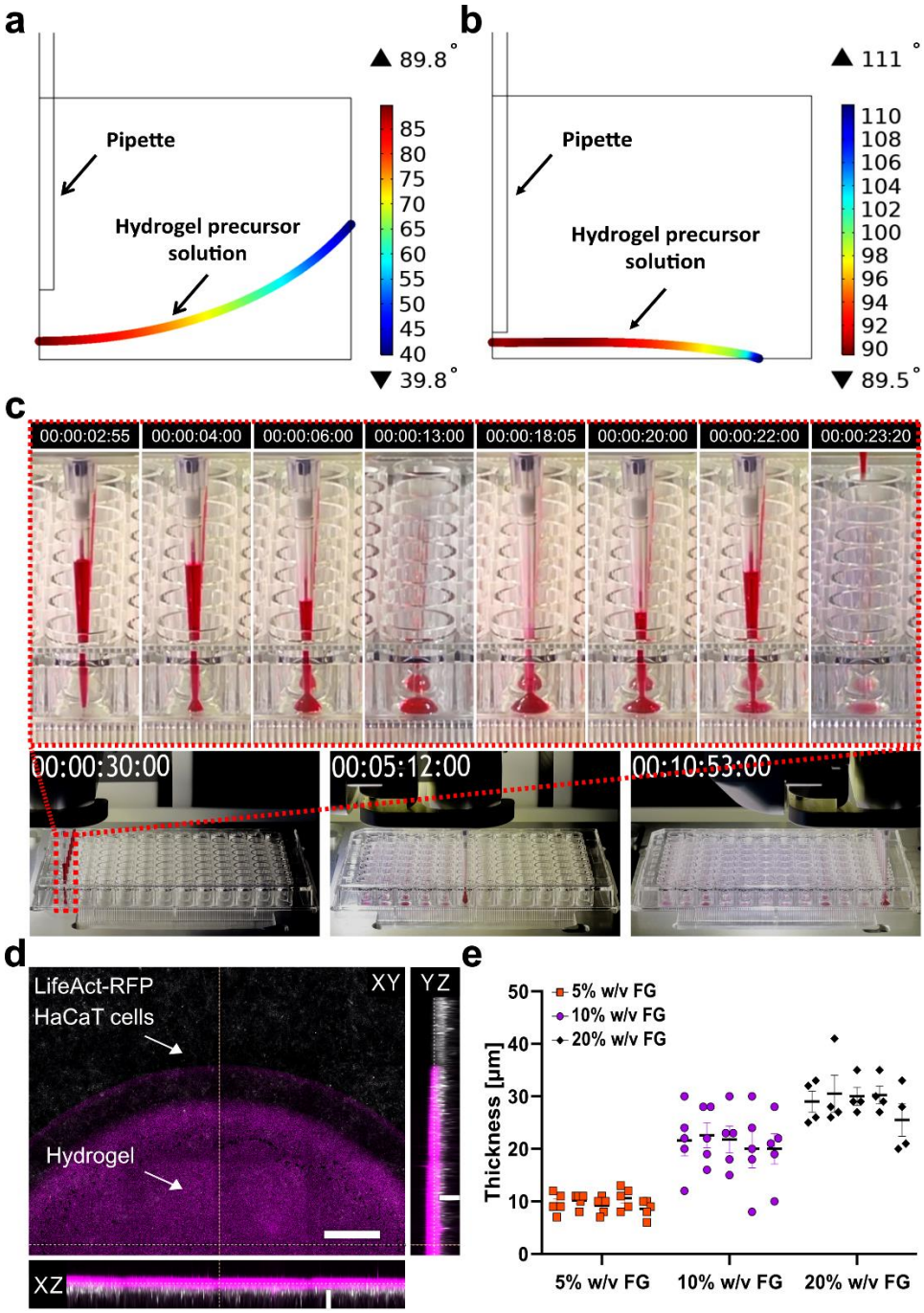

Fig. 3. Hydrogel Dispensing with Robotic Automation (HYDRA) fabrication method. 2D representation of hydrogel profile angles resulting from COMSOL simulation after (**a**) conventional casting, displaying meniscus formation, and (**b**) HYDRA casting. (**c**) Sequential frames illustrate the fabrication of FG hydrogel thin films using a commercial high throughput plate and liquid handling robot. Sequential frames of a zoom on a single well are displayed on top. (**d**) 2D reconstruction of hydrogel profile embedding fluorescent beads (in magenta) and with HaCaT cells (in gray – RFP-Life Act™) seeded on top. The z-stack of the hydrogel volume was acquired using confocal imaging. A max intensity projection was applied to the orthogonal views. XY plane scale bar: 200 µm. Orthogonal views (XZ, YZ) scale bars: 20 µm. (**e**) Assessment of thickness and flatness of FG hydrogels at three different concentrations (5% - orange squares, 10% - purple dots, and 20% w/v – black diamonds) in a hydrated state. The data corresponds to a single experiment (3 concentrations, n=5 samples for each concentration). For each sample, 5 FOVs were taken to measure the z-position and calculate thickness. Data are presented as mean ± s.e.m.

3.3 Drug testing using digital holographic for long-term imaging

To demonstrate HYDRA's utility in drug testing, we sparsely seeded HaCaT epithelial cells on gels and treated them with nocodazole and paclitaxel, two well-characterized cell cycle inhibitors[24,35,36]. The primary aim was to highlight the feasibility of integrating hydrogel-based cell culture platforms into imaging-based drug screening systems. As a stress test, we used long-term digital holography—an imaging method with minimal phototoxicity but sensitive to subtle refractive index shifts[37] to determine whether HYDRA's hydrogel layers interfered with detection. Having adding a thin hydrogel layer to provide a more biomimetic microenvironment for the cell with HYDRA, we asked whether digital holography could still pick up a sufficiently large refractive index change. Furthermore, we used cell culture plastic 96-well plates for this stress test, which have poorer optical properties than the HTS plates designed for imaging experiments. Digital holography experiments were conducted inside a cell culture incubator for 48 h.

We explored the range of drug concentrations known to affect the HaCaT cell cycle[35,36]. Specifically, we chose three concentrations of nocodazole (12.5, 25, and 50 ng mL^{-1}, shown in Fig. 4a-b-c) and three concentrations of paclitaxel (0.5, 2.5, and 12.5 ng mL^{-1} paclitaxel, as shown in Supplementary Fig. S6a-b-c). We included vehicle controls (0.1% DMSO in full culture media), where we expected no effect on the cell cycle, as well as positive controls, in which cells were exposed to a deadly concentration of an antibiotic to which HaCaT cells were not resistant (geneticin) (Supplementary Fig. S7a-b). In duplicate runs, cells were seeded either on FG gels or directly on plastic. We successfully imaged HYDRA-prepared gels using digital holography, capturing cell presence and morphology (Fig. 4a–c; Supplementary Figs. S6–S9; Movies S5–S6), extending phase microscopy to HTS formats[38].

Moreover, since we imaged all wells every hour for 48 h, we analyzed time-lapse images to measure the total area covered by cells, referred to as '% confluency.' This parameter is important because

proliferating cells increase their confluency over time, and compounds expected to arrest the cell cycle would ideally delay or arrest this increase (Fig. 4d, Supplementary Fig. S6d, S7a, and S9d-e).

After 48 h, nocodazole-treated cells showed distinct proliferation patterns on hydrogels versus plastic (Fig. 4e). Paclitaxel yielded similar trends (Supplementary Fig. S6e), and higher doses consistently reduced confluency across both substrates (Supplementary Fig. S7b). In these scenarios, the final cell confluences on the hydrogels were twice those observed on the plastic, highlighting the importance of more biomimetic substrates. We also quantified IC_{50} drugs in the case of plastic or hydrogel substrate: about 17 ng mL^{-1} on plastic and 18 ng mL^{-1} on hydrogel in the case of nocodazole, 1.6 ng mL^{-1} on plastic and 1.8 ng mL^{-1} on hydrogel in the case of paclitaxel (Fig. 4f and Supplementary Fig. S6 f). While yielding similar IC_{50} values, the proliferation kinetics of HaCaT cells on hydrogel or plastic differed, which is also in good agreement with the literature[18]. Together, these results support the notion that HYDRA HTS platforms can provide more biomimetic support for cell proliferation and can be integrated with advanced imaging capabilities and standard analysis pipelines for drug testing applications.

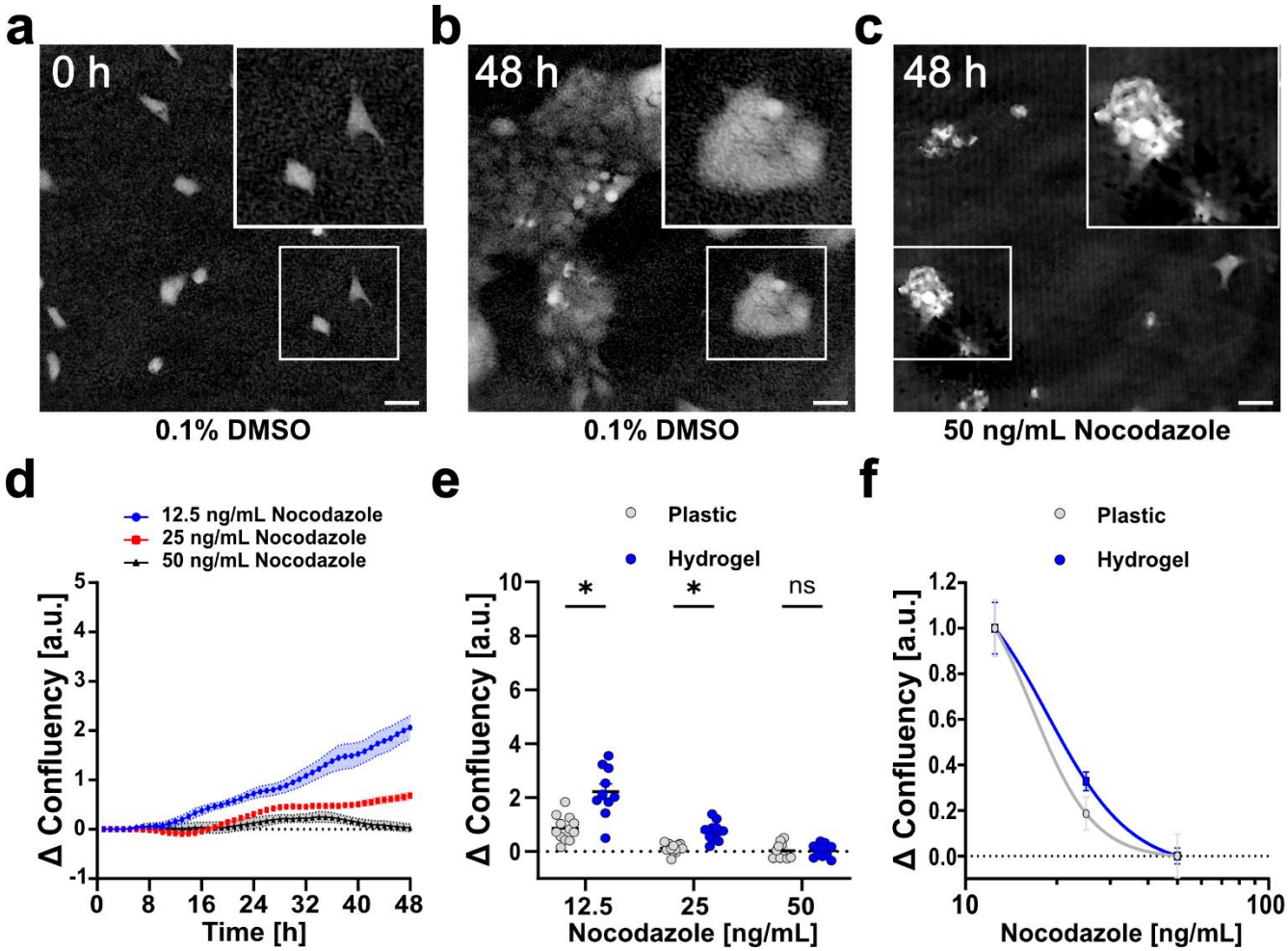

Fig. 4. Drug test using phase holographic imaging. (**a**) Holographic image of HaCaT cultured in 0.1% DMSO – vehicle control – after seeding and (**b**) 48 hours after seeding. (**c**) Holographic image of HaCaT treated with 50 ng mL^{-1} of nocodazole drug 48 hours after seeding. Scale bars: 50 µm. (**d**) HaCaT cell confluency vs. time. Cells were cultured in nocodazole-based cell culture media (12.5 ng mL^{-1} – blue dots, 25 ng mL^{-1} – red squares, 50 ng mL^{-1} black triangles) for 48 hours on hydrogel substrates. Data were normalized concerning the initial confluency value. Solid lines represent mean values, and shaded areas represent s.e.m (n=12). (**e**) Final cell confluency vs. nocodazole concentration (12.5 ng mL^{-1}, 25 ng mL^{-1}, 50 ng mL^{-1}) on plastic and hydrogel substrates. Data were normalized concerning the initial confluency value. (*) stands for significative difference. (**f**) Nocodazole dose-response curves on plastic (IC_{50}, 16.6 ng mL^{-1}) and hydrogel (IC_{50}, 18.1 ng mL^{-1}) substrates (n=12). Data were normalized concerning the initial confluency value (n=12). Image brightness and contrast were adjusted for printed visibility.

3.4 Drug testing assay using standard fluorescence static imaging

Next, we sought to validate the applicability of HYDRA plates to fluorescence microscopy and confirmed that the digital holography results obtained were consistent with the known mechanisms of action of the drugs used. Nocodazole and paclitaxel influence cell cycle progression by modulating microtubule dynamics, arresting the cell cycle before division (or M-phase), and eventually leading to cell death by apoptosis[39–41]. To examine the effects of these drugs on the cell cycle, we used HaCaT cells genetically engineered to express fluorescent sensors for the cytoskeletal proteins actin and tubulin as well as the cell cycle sensor FUCCIplex (Fig. 5a)[24]. This cell cycle sensor allowed us to determine the cell phases (Fig. 5b i-v).

In this set of experiments, we used fluorescence microscopy in a temperature- and CO_2-controlled incubator to repeat the same drug test performed using holographic imaging. Specifically, we used HYDRA to cast gelatin hydrogels onto plastic 96-well plates. We then counted M-phase-arrested cells on hydrogels or plastic in the presence of the two compounds 24 and 48 h after administration (Fig. 5b–iii, Supplementary Fig. S10–iii, and S11). First, we confirmed that fluorescence imaging is compatible with HYDRA-cast hydrogels, such as holographic imaging in the preceding section. Second, we examined evidence of drug effects.

Cells treated with the highest nocodazole drug concentration displayed nuclear fragmentation (Fig. 5b iv), typically associated with cellular damage before apoptosis[42]. For this reason, cells with a nuclear area smaller than the mean nuclear area of control cells were excluded from the analysis. By counting the fraction of cells undergoing cell division, we showed the expected dose-dependent accumulation of arrested cells in the nocodazole-treated group (Fig. 5b - v)[35,36]. Furthermore, we observed nuclear fragmentation (Supplementary Fig. S10 - iv) and a comparable trend in the number of cells undergoing mitosis in paclitaxel-treated samples (Supplementary Fig. S10 - v)[42].

281

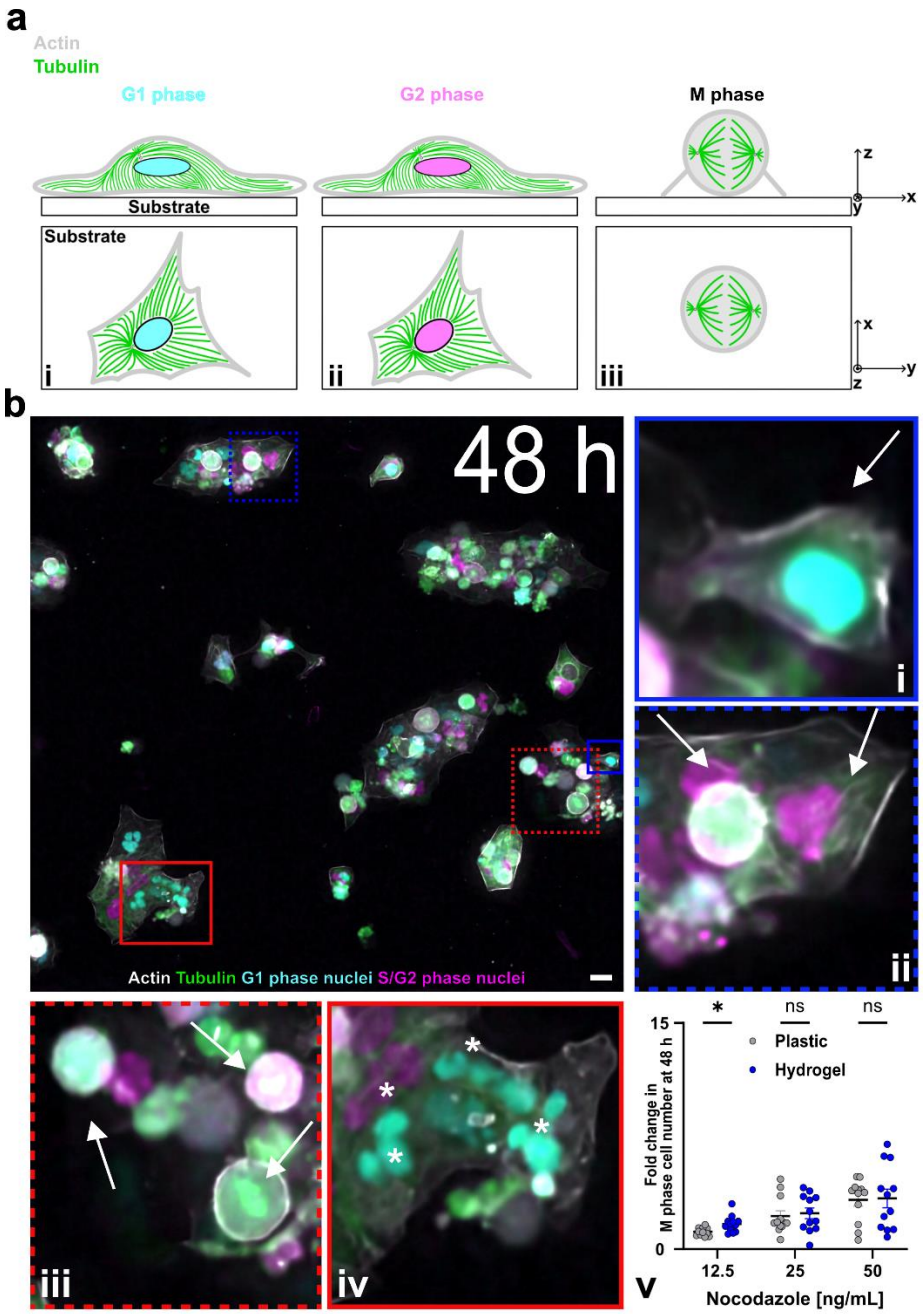

Fig. 5. Drug test using fluorescence imaging on HYDRA hydrogels cast on inexpensive traditional tissue culture plastic. This is a worst-case configuration for imaging because photons must travel through a thick polystyrene layer in addition to the thin hydrogel layer (see Fig. 6 for a best-case scenario). (**a**) Schematic illustration of cell-substrate interaction during the cell cycle. A cell in i) G1 or in ii) S/G2 phase exhibits a degree of spreading based on the substrate. During iii) the mitosis (M) phase, the phase before cell division, the cell undergoes rapid internal architectural changes, assuming the characteristic spherical shape associated with mitotic cells. (**b**) Static widefield images of HaCaT (RFP – Life Act in gray, GFP – tagged tubulin in green) 48 hours after seeding on gels cast on tissue culture plastic. Cells were treated with 50 ng mL^{-1} nocodazole. Arrows stand for (i) cells in the G1 phase (in cyan), (ii) cells in the S/G2 phase (in magenta), and (iii) cells in the mitotic (M) phase. Asterisks stand for (iv) nuclear fragmentation. (v) Fold change in M phase cell number after 48 hours vs. nocodazole concentration on plastic and hydrogel substrates. Cell number in the M phase was counted as a fraction of the total cell number in a FOV and then normalized to the vehicle negative control (n=12). Data are displayed as mean ± s.e.m. (*) stands for statistical difference. Images were taken on hydrogel thin layers cast on plastic plates. Scale bar: 25 μm.

3.5 HYDRA compatibility with very high throughput formats

Finally, we investigated whether the HYDRA method could be scaled to other high-throughput formats, such as a 384-well plate, and higher-resolution imaging modalities using plates with a high-refractive-index cyclic olefin copolymer (COC) backing. With a working volume of 1 µL, HYDRA prevented meniscus formation by preventing contact with the walls of each well. With such a small volume, we used 10% w/v FG and 0.5% w/v TG to reduce precursor viscosity and optimize dispensing so that the entire plate could be completed in approximately 10 min. Given the large number of prepared wells, we developed an automated quality control procedure for HYDRA plates that acquired and analyzed 384 wells in less than two hours (Fig. 6a and Supplementary Movies S7 and S8). First, we took fluorescence images of the embedded beads with a 4X objective (NA 0.13) in the confocal mode. Second, we calculated the maximum intensity projections to determine whether the gel touched the walls (red box) or if the intensities were inhomogeneous (yellow box). Our quality control revealed a yield of ~90% (green box) with only 6% unusable meniscus profiles (Fig. 6a, red box) and partially usable concave gels (yellow box) (Fig. 6a). We further characterized a sample of inhomogeneous gels with higher-resolution Z-stacks to confirm their non-planar profiles (Supplementary Fig. S12a-b). In contrast, 1536-well plates yielded <10% usable gels, due to robotic limitations in volume handling and positioning accuracy (Supplementary Fig. S12c).

Finally, we demonstrated how HYDRA 384 well plates can be used in advanced fluorescence microscopy applications as required by modern imaging-based HTS approaches (Fig. 6 b)[43]. First, we performed live-cell imaging experiments by following HaCaT cell proliferation for 18 hours on multiple fields-of-view using a 40x silicon oil objective (NA 1.25) and a perfect focus system (Fig. 6c and Supplementary Movie S9). The image quality was high enough to enable semi-automated segmentation and tracking with

modern AI-based image analysis software, such as Stardist and TrackMate (Fig. 6c)[44,45]. Finally, to show that the gels did not prevent the assessment of fine ultrastructural details, we performed high-resolution confocal acquisitions with a 100X silicon oil objective (NA 1.35) (Fig. 6d). In the same field of view, we could observe how microtubule organization changes from a mostly planar network in adhered and spread-out cells (Fig. 6d - i) to a mitotic spindle during cell division (Fig. 6d - ii). Together, our results show that HYDRA can be used in various well-plate formats, from low throughput to HTS, and substrates, from glass to plastic, where it remains viable for two months (Supplementary Fig. S13). In all of these scenarios, HYDRA enables HTS with multiple imaging modalities.

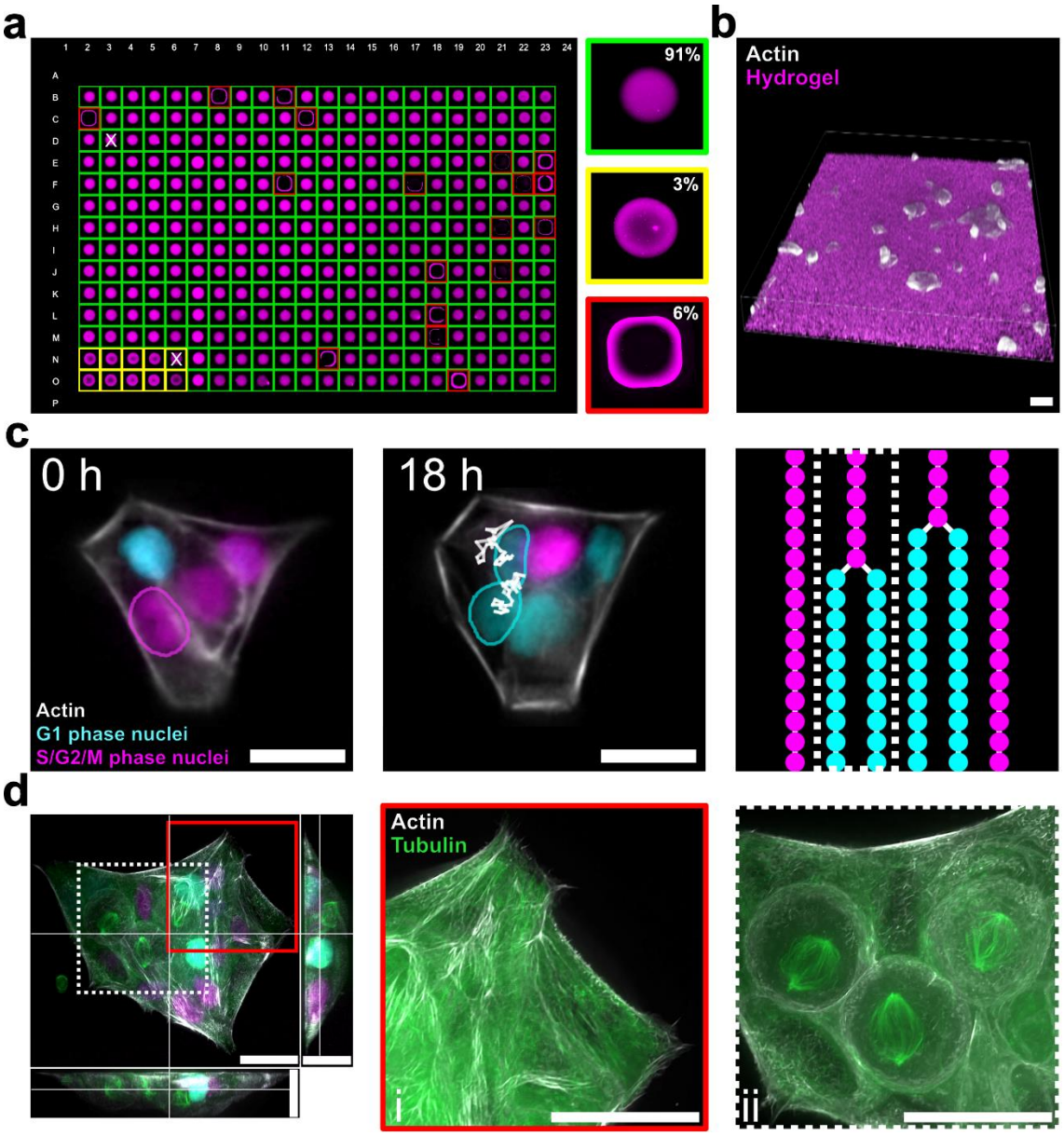

Fig. 6. HYDRA-like hydrogels on an imaging-grade 384-well plate. (**a**) Hydrogels were cast in a 384-well plate by using 10% w/v FG/0.5% w/v TG. Hydrogel precursor solutions were mixed with fluorescent beads (shown in magenta) to visualize the gel volume. An automatic quality control analysis was performed to evaluate hydrogel morphology and check if the sample touched the well walls. 91% of the samples resulted in well-deposited planar hydrogels (green boxes), 6% of them formed a meniscus due to touching the walls (red boxes), while 3% of samples appeared with a concave shape (yellow boxes). "x" symbols on well shows wrong classification done by the automatic analysis. Well width: 3.7 mm. (**b**) 3D rendering of HaCaT cells (actin in grey) on the hydrogel surface (fluorescent beads in magenta). (**c**) 18-hour live fluorescence imaging experiment of HaCaT cells on hydrogels. HaCaT cells express fluorescent sensors for actin (in grey) and the cell cycle (cyan nuclei in G1 phase in cyan, nuclei in S/G2/M phase in magenta). Segmentation masks for selected cells and tracks backward in time are shown. Mask outlines were colored manually on TrackMate according to the cell cycle phase. A tracking diagram is shown where each spot represents a cell at a specific phase of the cell cycle at each time point. The dashed white box indicates the tracking lineage of the highlighted cells. (**d**) Max intensity projections of the XY, XZ, and YZ planes from a z-stack showing a cluster of cells on hydrogels (actin in grey, tubulin in green, nuclei in cyan and magenta). (**i**) The Red squared box zooms in on three cells undergoing mitosis, evidenced by mitotic spindles in green. (**ii**) The white dashed box shows the actin and tubulin structures of cells well spread on the hydrogel surface. Zooms were adjusted by applying a Sharpening filter in FIJI[30]. Scale bars: 25 µm.

4. Discussion

In this study, we asked, "What would it look like if it were simple to have biomimetic elements in HTS?" Existing solutions for biomimetic functionalization of multi-well plates either yield layers too thin to mask substrate stiffness or too thick for high-resolution imaging.[20,21] Our answer is HYDRA, which is a scalable and automated approach for fabricating thin hydrogel films at the bottom of commercial HTS plates. To do so, throughout this study, we sought material composition and fabrication strategies that would be simple to implement not only in academic research frameworks but also in industry-level scenarios.

We selected gelatin for its mild surfactant properties, which enable contact-line pinning and allow excess precursor to be removed during re-aspiration—yielding planar, micrometric-thick hydrogels[46]. We specifically chose cold fish gelatin (Fig. 2a, 2e-f) instead of the more commonly used mammalian gelatins. Mammalian gelatin is utilized in manual casting or 3D printing because of its viscous nature at RT, which can be further tuned with a temperature-controlled print-head[27]. While we could have adopted a similar strategy, we preferred standard liquid-handling equipment and sought a gelatin composition that would remain liquid at RT. Although fish and mammalian collagens have several differences in their tertiary and quaternary structures, their denatured products, gelatins, are much more similar[27,28]. Our rheological studies demonstrated that the viscosity of fish gelatin at RT could be effectively handled using air displacement pipettes, even at elevated protein concentrations (Fig. 2b). Moreover, the dispensed layer can be effectively cross-linked by microbial TG within a physiological range of stiffness (Fig. 2e-f). This suggests that this strategy can be used as is in applications with a desired cell-adhesive hydrogel. However, our method could be extended to other materials with liquid hydrogel precursors (also photocrosslinkable) to adjust the hydrogel stiffness and cell-binding properties, such as hyaluronic acid, alginate, or methacryloyl fish gelatin[47–49].

We approached the fabrication process similarly: "What could be the easiest way to cast hydrogels in HTS plates for the pharmaceutical industry?" The HYDRA manufacturing process is simple and involves the dispensing of a small volume of the hydrogel precursor solution at the center of each well, followed by re-aspiration of the same liquid volume (Fig. 1a-b). After dispensing the liquid and wetting the well bottom, a small amount of the hydrogel precursor remained adhered to the glass/plastic, ensuring that a thin hydrogel layer could be crosslinked in place. Here, the HYDRA method was demonstrated by considering the wells of standard 96- (Fig. 3) and 384-well plates (Fig. 6) with minimal hydrogel modifications. 1536-well formats should also be feasible with more precise robotics that prevent wall contact and retain a boundary layer after reaspiration.

Next, we sought to validate HYDRA in challenging applications from a microscopy standpoint. We reasoned that introducing a hydrogel layer could impact imaging performance and placed ourselves in the most pessimistic scenario by casting the gelatin hydrogel in a plastic 96-well plate. Even under these conditions, we demonstrated the suitability of HYDRA HTS plates for digital holography (Fig. 4) and fluorescence microscopy (Fig. 5) on human epithelial cells engineered with various fluorescent sensors and treated with two drugs. Finally, we used imaging-grade 384-well plates with COC backing to perform advanced live-cell and high-resolution confocal imaging of cells cultured on HYDRA gels (Fig. 6c-d). The extra layer at the bottom of the plate did not affect the standard imaging instruments, and the data quality was sufficient to automate data analysis in ways similar to current state-of-the-art cell painting assays and image analysis pipelines[16,17].

The main limitation of HYDRA is the residual glass/plastic rim at the edge of the gel. This strong edge effect can easily be addressed in imaging experiments by acquiring data only from the gel area. However, the presence of cells on the glass/plastic rim remains problematic when extracting DNA, RNA, or proteins from the well, as the cells outside the gel may have properties distinct from those on the gel.

Compared to the layer-by-layer and photo-crosslinking approaches for obtaining hydrogels in HTS plates, we traded good coverage in favor of physiologically relevant thickness and high-res imaging compatibility[20,21]. Because the final plate remains optically and chemically addressable, combining these and other approaches to generate full-well, more complex microenvironments in future versions of HYDRA will be possible[47–49].

5. Conclusion

We developed HYDRA, a fully automated protocol for fabricating thin planar hydrogels in standard HTS well plates. We used microbial transglutaminase-crosslinked fish gelatin as a cost-effective solution to create tissue-mimicking environments with tunable gel properties and high compatibility with automated liquid handling. We obtained planar gel profiles by exploiting the contact angle hysteresis during liquid re-aspiration and surface dewetting. We validated this approach using imaging technologies and bioimage analyses that are relevant to HTS. Our approach can be easily integrated into a standard pharmaceutical pipeline as it uses nothing but readily available instruments and reagents in their expected context of use. Therefore, HYDRA has the potential to significantly improve the predictivity of preclinical trials for drugs R&D by providing better mimicking substrates with a cost-effective and HTS-ready solution.

2. Materials and methods

2.1 Preparation of transglutaminase-crosslinked fish gelatin hydrogels

Gelatin from cold water fish skin (FG) (G7041-500G, Merck) was dissolved in Dulbecco's phosphate-buffered saline (PBS) without Ca^{2+} and Mg^{2+} (referred to as "PBS -/-," C-40232, PromoCell) at 50°C under magnetic stirring (700 rpm) for 30 min and filtered through a 0.45 µm filter (514-1265, VWR). Transglutaminase (TG) powder (Activa® TI Transglutaminase, 1002, Modernist Pantry) was dissolved in PBS -/-, vortexed (between 700 and 800 rpm) for 10 min, and then filtered through a 0.45 µm filter. FG and TG solutions were used fresh or stored at 4 °C for up to one week. To explore the thickness and flatness of robot-cast hydrogels, samples were prepared with a gelatin content of 0.2 g mL^{-1} (20% w/v), 0.1 g mL^{-1} (10% w/v), and 0.05 g mL^{-1} (5% w/v) while keeping a constant TG concentration of 0.02 g mL^{-1} (2% w/v). For 5% and 10% gels, 1:1 mixes of 10% and 20% FG stock solutions with 4% TG were used, respectively. A 4:1 mix of 25% FG and 10% TG yielded 20% gels. After mixing, the resulting hydrogel precursor solution was placed in a cell incubator (37 °C, 90% relative humidity, 5% CO_2) for overnight crosslinking. During crosslinking in the incubator, a water reservoir was placed with the plate in a sealed box in an incubator to maintain relative humidity control. Prior to cell culture, hydrogels were sterilized for one hour using a cell culture hood's ultraviolet (UV) light, then immersed in PBS -/- for at least 6 h to allow for swelling, and then rinsed three times in PBS -/- to remove transglutaminase and ammonia byproducts. To cast the hydrogels in 384- (781866, GREINER) and 1536-well plates (4561, Corning), a precursor solution containing 10% w/v FG, and 0.5% w/v TG was prepared.

2.2 Rheological characterization of hydrogel viscosity and stiffness

Gelation of fish gelatin (FG) was assessed by tube inversion using 5%, 10%, and 20% (w/v) FG solutions in PBS -/- pre-mixed with TG[28]. Samples (n = 3) were incubated at room temperature or 4 °C for 72 hours, and tube inversion was recorded at 24, 48, and 72 hours. Rheological measurements were performed using a Discovery HR-2 rheometer (TA Instruments) with a plate-plate geometry and a Peltier solvent trap to prevent water evaporation. To verify compatibility with automated pipetting, the viscosity of the hydrogel precursors (5-20% w/v) was characterized by flow sweep measurements at room temperature by pipetting 150 µL of FG solution directly onto the plate. To assess the shear modulus (stiffness), samples were firstly crosslinked overnight at 37 °C. Hydrogels with varying FG concentrations were shaped into cylinders approximately 2 mm in height and 2 cm in diameter. The cylinders were prepared by casting the hydrogel precursor solution on a glass microscope slide and shaped into cylinders using glass coverslips as lateral spacers and a passivated coverslip on the top. Time sweep measurements were carried out at constant strain (1%) and frequency (1 Hz) at 37 °C. Dynamic amplitude measurements were performed at a constant frequency (1 Hz), at increasing strain (0.1-1000%), at 37 °C. Gelation measurements were performed on hydrogel precursor formulations by pipetting 150 µL of solution onto the plate (strain 1%, frequency 1 Hz).

2.3 Computational Fluid Dynamics Simulations

COMSOL Multiphysics (version 6.1, COMSOL) was used to explore the possibility of producing planar 2.5D hydrogels by simulating the dispensing and aspiration processes using a pipette tip in the center of a cylindrical well. The "Laminar Two-Phase Flow, Phase Field" interface (including gravity contribution) was used to track the air-liquid interface. Exploiting the axial symmetry of the system (pipette at the center of a well), a 2D axisymmetric geometry was chosen to save computational power and time. The well was modeled as a rectangle of dimensions Rw and Hw (Table S1), with "wetted wall boundary" conditions imposed for the bottom and sidewall boundaries of the well and "open boundary" conditions at the top of the well, as the upper part of the well is open. In the "wetted wall" condition, the contact angle hysteresis was modeled using advancing and receding angle values reported in the literature to capture the surfactant properties of gelatin and the resulting contact angle hysteresis (Table S1)[50]. Specifically, the angle at the wetted wall was set as "advancing" when the contact line velocity, the velocity at which the fluid moves at the bottom of the well, was positive and as "receding" when it was negative. The pipette was modeled as a rectangle (Rp and Hp, Table S1), with an "interior wetted wall" condition at the lateral wall of the pipette inside the well domain. An "inlet" condition was applied at the upper edge of the pipette to simulate dispensing and aspiration by using positive and negative "fully developed flow," respectively. Material properties were set using COMSOL library for air and water, and were assigned to the well and pipette domains, respectively. To model the hydrogel precursor solution at the selected COMSOL interface, the viscosity of the liquid phase was set to the value for the 10% w/v hydrogel precursor solution found in this study. The density and surface tension were set at the nominal value for water and the value found in the literature for FG[46]. The mesh was created using the "physics-controlled" option with an "extra fine" option for mesh size. Gel flatness was assessed by evaluating the angle at every profile point, which was directly calculated using COMSOL software. The

air-liquid interface was considered “planar” when the angle concerning the pipette axis was 90° ± 3°. Flatness was calculated as the percentage of the length of the “planar” air-liquid interface over the well radius. Wall wetting was evaluated via a parametric sweep varying the dispensed volume by ±20% and reducing the well radius by 100 or 200 µm to account for plate tolerance and robot calibration errors.

2.4 Robotic hydrogel fabrication

An open-source pipetting system (OT-2 robot, Opentrons) was used to fabricate micrometer-thick planar hydrogels. Specifically, a liquid handling robot pipeline was implemented using the Opentrons Protocol Designer (Version 7.0.0, Opentrons) to cast and re-aspirate the hydrogel precursor solutions, leaving planar cylindrical hydrogels on the plastic substrates. In terms of hardware, removable P300 single-channel Gen2 pipette (in short “P300") and a P20 single-channel Gen2 pipette (in short “P20”), an Eppendorf vial rack for the stock solutions (Opentrons), and 8-well plates (µ-Slide 8 Well High ibiTreat, 80806, Ibidi) as receiving plastic substrate were used. Before casting, the system was calibrated to account for pipette lengths and hardware positions. During casting, the FG and TG stock solutions were mixed into a new vial using P300, using individual tips. The hydrogel solution was then cast into an 8-well plate using an individual P20 tip for each gel. Specifically, the pipette was programmed to dispense 12 µL of liquid at 500 µm from the well bottom with a flow rate of 0.5 µL s^{-1} and aspirate the same volume at 100 µm from the well bottom with a flow rate of 0.1 µL s^{-1}. To test the HYDRA in low-throughput plates, a custom protocol in Python was developed using P300 and P20 pipettes, an Eppendorf tube rack for the stock solutions (Opentrons), and 12-well plates (11012, BIOFIL) as the plastic substrate. Initially, the precursor solutions were premixed in a new tube rack using a P300 pipette. HYDRA-like hydrogels were cast in the first half of a 12-well plate using a volume of 200 µL each. After re-mixing the precursor solutions, a P20 pipette was used to cast multiple 20 µL gels in each well of the second half of the plate. To visualize the final gel, 18 µL volume was aspirated from each gel.

2.5 Scalable hydrogel fabrication using a multichannel system

FG hydrogels were fabricated in 96-well plates using an Assist Plus robot with a 3-position deck (4520, Integra Biosciences) to enable scalable hydrogel production. Two 8-channel pipettes were used, namely 300 µL and 12.5 µL 8-channel VOYAGER pipettes (respectively, 4723 and 4721, Integra Biosciences). Two sequential protocols were developed using the VIALAB software (Version 3.1.2.0, Integra Biosciences). First, FG and TG solutions were mixed and dispensed into an 8-row set of Eppendorf vials using the 300 µL pipette. The pipette was then replaced manually with the 12.5 µL model to dispense 12 µL of precursor solution into a 96-well plate (83.3924, Sarstedt), followed by re-aspiration in one column at a time. A pre-mixing step was included before dispensing. Two additional 96-well plates (89626, IBIDI) were prepared similarly to assess long-term hydrogel stability. After crosslinking, the plates were rehydrated in PBS, sealed with parafilm (PM-992, Bemis), and stored at 4 °C for up to two months. Engineered HaCaT cells expressing a fluorescent marker for actin were seeded on the gels to assess hydrogel degradation after one and two months. Static widefield images were captured using a Crest V3 X-Light spinning disk confocal microscope (Nikon) equipped with a Celesta Light Engine source (TSX5030FV, Lumencore), Photometrics Kinetix Scientific CMOS camera, and an air 10x objective (NA 0.30) (MRH00105, Nikon). During acquisition, a Lumencore CELESTA Light Engine source was used to illuminate the sample through the 10x objective at a wavelength of 546 nm for 200 ms with a laser power of 16 ± 2 mW. One field of view per well was automatically acquired using the JOBS module in NIS-Elements[51].

For higher-density formats, a 16-channel VIAFLO pipette (12.5 µL, 4641, Integra Biosciences) was used to dispense hydrogels into 384-well (781866, Greiner; 4681, Corning) and 1536-well plates (4561, Corning). A 10% FG / 0.5% TG solution was pre-mixed in a 25 mL reservoir (4310, Integra Biosciences),

then 1 µL and 0.5 µL were dispensed into 384- and 1536-well plates, respectively, followed by a 0.5 µL aspiration.

To promote adhesion on glass surfaces, a previously reported silanization protocol for glass coverslips[25] was adapted to 96-well plates with a glass bottom (89627, IBIDI) using an OT-2 robot (Opentrons) under a chemical hood. and Opentrons Protocol Designer (Version 7.0.0, Opentrons). Wells were sequentially treated with 0.1 M NaOH (5 min; 1.09137.1000, Sigma), 0.5% APTMS in ethanol (5 min; 313251000, Thermo Fisher), and 0.5% glutaraldehyde (30 min; 8.20603.0100, Sigma). Static BF images (5 ms exposure) were captured using the same confocal setup with an air 4x objective (NA 0.13, MRH00045) to image the entire gel. Image acquisition was automated via NIS-Elements JOBS[51] and Flat-field correction was applied using the BioVoxxel 3D Box plugin in FIJI[44].

2.6 Cell culture

HaCaT cells were genetically engineered to express multiple fluorescent markers, including FUCCIplex (mTurquoise2 and miRFP670) for cell cycle tracking, RFP-LifeAct™ for actin, and EGFP-tagged tubulin for microtubules, following a previously established protocol[24]. The engineered HaCaT cells were cultured in a conventional incubator (37 °C, 90% relative humidity, 5% CO_2) using Dulbecco's modified Eagle's medium F-12 Nutrient Mixture (DMEM F-12, 11320-074, Gibco), supplemented with 10% heat-inactivated fetal bovine serum (10270-106, Gibco) and 1% penicillin and streptomycin antibiotic solution (A001-100ML, Himedia). Cultures were maintained below confluency and split at 70% confluence.

2.7 Morphological characterization of robot-cast gels in hydrated states

To evaluate the geometry of the hydrogels in the hydrated state, fluorescent beads (excitation 660 nm/emission 680 nm, F8807, Thermo Fisher) were added to the precursor solution at a 50:1 ratio.

Hydrogels with 5%, 10%, and 20% w/v gelatin were cast into an 8-well plate (80806, Ibidi), crosslinked overnight, and rehydrated in PBS -/- before cell seeding. To verify the biocompatibility of the hydrogel and characterize the hydrogel profile by fluorescence confocal microscopy, $5x10^5$ cells mL^{-1} genome-edited HaCaT cells were seeded. The RFP-Life Act™ construct (excited at 546 nm) was used for this experiment to visualize actin and obtain fiduciary points for assessing the gel profile and plastic substrate. Static confocal images were captured on both the upper and lower surfaces of the gels using a Crest V3 X-Light spinning disk confocal microscope (Nikon) with a Celesta Light Engine source (TSX5030FV, Lumencore), a Photometrics Kinetix Scientific CMOS camera, and air 20x objective (NA 0.75, MRD00205). The z-level of the cells adhering on top of the gel and of the plastic substrate was recorded to evaluate the gel thickness and flatness.

2.8 Drug screening using digital holographic long-term imaging

Nocodazole (M1404-50MG, Merck) and paclitaxel (10461, Cayman Chemical) were chosen as test compounds. Stock solutions (5 mg mL^{-1} in dimethylsulfoxide, D2650-100ML, Merck) were aliquoted in 1 mL Eppendorf tubes and stored at -20 °C. HaCaT cells (P50-P70, 5 x 10^4 cells mL^{-1}) were seeded on 10% w/v FG hydrogels 24 h before treatment. Cells were exposed to three concentrations of each drug: 12.5, 25, and 50 ng mL^{-1} for nocodazole; 0.5, 2.5, and 12.5 ng mL^{-1} for paclitaxel. Controls included 0.1% DMSO (negative) and 1500 µg mL^{-1} Geneticin (10131-027, Gibco; positive), with 12 replicates per group. After adding drugs, the 96-well plate was immediately placed on the motorized stage of a HoloMonitor M4 (Phase Holographic Imaging AB) inside a cell incubator (37 °C, 90% relative humidity, 5% CO_2). Using HoloMonitor Appsuite software (Version 4.0.1, Phase Holographic Imaging PHI AB), one field of view per well was imaged every hour for 48 h using an Olympus PLN 20x objective (NA 0.4) (N1215900, Evident) and a low-power laser unit (635 nm, 0.2 mW cm^{-2}). Time-lapse images were

analyzed in FIJI to calculate cell confluency, defined as the ratio between the area covered by cells and the total field of view.

2.9 Drug screening using static widefield fluorescence imaging

Complementary to the holographic assay, a 96-well platform was used to capture static widefield images of cells on the gels at 24 and 48 h after drug treatment. One image per well was captured using a Ti2 inverted microscope (Nikon) equipped with an air 20x objective (NA 0.75, MRD00205). Lumencore CELESTA Light Engine with 546 nm (laser power 16 ± 2 mW, exposure 50 ms), 477 nm (28 ± 3 mW, 50 ms), 446 nm (20 ± 2 mW, 10 ms), and 638 nm (37 ± 4 mW, 200 ms) wavelengths was used to image cell actin, tubulin, and nuclei in G1 and S/G2/M, respectively. The semi-automated imaging protocol was implemented using the JOBS module in Nikon NIS-Elements. For each well, the objective was positioned at the center, the focus was manually adjusted at 477 nm, and 4-channel images were recorded. The entire protocol was executed twice: first to capture cells on hydrogel substrates, and then to acquire cells on the plastic rim surrounding the gel.

2.10 Cell confluency analysis using digital holographic long-term imaging

Cell confluency, defined as the percentage of the field of view occupied by cells, was extracted from time-lapse images acquired with the HoloMonitor M4. Datasets were exported from HoloMonitor Appsuite (Version 4.0.1, Phase Holographic Imaging) and processed using FIJI[44]. The images were processed as follows: “Non-local means (NML) denoising” ImageJ plugin (auto-estimated sigma, smoothing factor “1”)[52,53], Auto-threshold (“Triangle” method, default settings provided by ImageJ), morphological operators including “Opening,” “Closing” and “Filling holes” operators (ImageJ) and Particle analysis (“Analyze Particles” ImageJ plugin) to extract “%Area” values, i.e., cell confluency values. To reduce quantitative phase imaging artifacts, a moving average (window size = 4) was applied

to time-series data. For frames exceeding 30% confluency, manual adjustments were required due to reduced accuracy of automatic segmentation.

2.11 Automated quality control of HYDRA-like hydrogels in HTS plates

Automated acquisition and quality control analyses were performed to evaluate hydrogel fabrication in 384-well (781866, GREINER) and 1536-well (4561, Corning) plates. Using the JOBS module in Nikon NIS-Elements, static widefield z-stacks (30 µm z-step size) were automatically acquired at the center of each well with a Crest V3 X-Light spinning disk confocal microscope (Nikon) equipped with a Celesta Light Engine source (TSX5030FV, Lumencore), a Photometrics Kinetix Scientific CMOS camera, and an air 4x (NA 0.13, MRH00045). Illumination was provided at 546 nm (16 ± 2 mW, 300 ms) and 638 nm (37 ± 4 mW, 30 ms) wavelengths to image well walls and hydrogels embedding fluorescent beads, respectively. A custom FIJI macro script was used to process the 2-channel z-stacks. Briefly, each image was cropped and rotated to center the well within the field of view. The maximum intensity projection was then obtained from the 2-channel stack input. In the well wall channel, gamma correction (0.5), auto-thresholding ("Triangle"), morphological operations (opening, closing, hole filling), outlier removal (radius 10 px), and edge detection were applied. The hydrogel channel underwent similar processing, using the "Default" threshold method. A logical AND operation between the hydrogel and well wall masks identified gels in contact with the well edges ("bad"). A secondary analysis on the hydrogel projection (gamma = 2, auto-threshold, closing) classified gel shape based on mean gray value: ≥250 was defined as "planar," otherwise "concave." Well classifications ("bad," "planar," "concave") were saved in an Excel file. A Python script then tiled the processed images by classification, overlaying each well with a colored frame: green (planar), red (wall contact), or yellow (concave).

2.12 Profile extraction of fish gelatin hydrogels in a 384-well plate

To assess hydrogel profiles in 384-well plates (781866, Greiner), fluorescent beads were embedded in the gel matrix as previously described. After overnight crosslinking and rehydration in PBS -/-, large field-of-view confocal z-stacks were acquired using a Crest V3 X-Light spinning disk microscope (Nikon) equipped with a Celesta Light Engine (TSX5030FV, Lumencore), a Photometrics Kinetix CMOS camera, and a 20x air objective (NA 0.75, MRD00205). A custom Python script was developed to extract profiles from n=3 for concave and n = 5 for planar gels. Briefly, z-stack images were processed by applying Otsu thresholding and morphological closing to differentiate the gel from the background. Gel height was determined by the distance between the first and last detected signals, multiplied by a 2 µm z-step size. Profiles were smoothed using a 15-pixel moving average filter (~10 µm, pixel size = 0.67 µm).

2.13 High-resolution live fluorescence imaging

Cells on gels cast in 384-well plates (4681, Corning) were analyzed using long-term widefield acquisition and static confocal fluorescence imaging. For long-term widefield imaging, one image per well was taken every 15 min for 18 h. Three wells per plate were considered. A Ti2 inverted microscope (Nikon) was equipped with a 40x silicon oil objective (NA 1.25) (MRD73400, Nikon). Lumencore CELESTA Light Engine with 546 nm (16 ± 2 mW, 200 ms), 477 nm (28 ± 3 mW, 30 ms), 446 nm (20 ± 2 mW, 10 ms), and 638 nm (37 ± 4 mW, 60 ms) wavelengths was used to image cell actin, tubulin, and nuclei in G1 and S/G2/M, respectively. For high-resolution static imaging of cell clusters, confocal z-stacks (0.3 µm z-step size) were captured using a Crest V3 X-Light spinning disk confocal microscope (Nikon) equipped with a Celesta Light Engine source (TSX5030FV, Lumencore), Photometrics Kinetix Scientific CMOS camera, and a 40x (NA 1.25, MRD73400) or 100x silicon oil objective (NA 1.35, MRD73950). Z-stacks were processed using AI Denoising and Richardson–Lucy deconvolution (50 iterations) in NIS-Elements

software, and visualized as XY maximum intensity projections, orthogonal views (XZ, YZ), or 3D renderings.

2.14 Cell cycle analysis using fluorescence widefield imaging

Cell cycle analysis was conducted on both long-term time-lapse and static widefield fluorescence images. In both cases, nuclei were classified using FUCCI-based markers, as previously reported[24]. Briefly, the cyan (G1) and magenta (S/G2/M) channels were denoised (non-local means[52] or median filtering), combined, and segmented using the pre-trained StarDist model (Versatile fluorescent nuclei)[45]. ROIs were extracted, and cells were classified into early G1 (no signal), G1 (cyan signal above threshold), S/G2/M (magenta signal above threshold), or transition (T; both signals above threshold), following background subtraction and intensity thresholding. Segmentation masks were manually curated when necessary (~10% of frames). For static images, mitotic cells were additionally identified using the tubulin (green) channel. After removing cyan signal to correct for bleed-through, tubulin intensity was measured within nuclei. The background was estimated from the surrounding cytoplasm. A cell was classified as mitotic if tubulin intensity exceeded background by ≥0.2 (plastic) or ≥0.4 (hydrogel). These predetermined values were established to automate the classification analysis, similar to a manual evaluation from an expert. Notably, the tubulin threshold for cells on hydrogel was doubled in value compared to that of cells on plastic to account for the autofluorescence background from the gel. In time-lapse data, segmented label images were imported into TrackMate[54]. The LAP tracker was used (50 μm max distance, 3-frame gap closing), with nuclear intensity-based penalties. Lineage trees were generated with phase-specific colour coding[55]. The linking of daughter cells was performed manually. Manual corrections (~5%) were applied to recover daughter cells after mitosis, when FUCCI signals were briefly absent.

2.15 Statistical analysis and software

Statistical analyses were performed using GraphPad Prism 10 software (GraphPad Software, USA). Mann–Whitney multiple tests were performed to compare confluency in long-term time series and static images. All results are presented as the mean ± standard error of the mean (s.e.m.). The conceptual drawing of the liquid-handling robot in the table of contents graphic was created in BioRender. (Di Sante, M. (2025) https://BioRender.com/ e23i519.)

Author contributions

E.T. and F.S.P. contributed equally to this work. E.T. and F.S.P. conceived and demonstrated the concept of fabricating HYDRA-fabricated hydrogel thin films in high-throughput plates. E.T. conducted all characterization of the HYDRA method, managed cell handling, performed drug testing and long-term imaging experiments, and analyzed the data. M.D.S. provided the engineered cells used in the experiments. M.M. and J.U.L. conducted rheological measurements of fish gelatin. B.H., A.E., and E.C. designed and conducted the COMSOL simulations for casting gels in high-throughput wells. M.P. created the code to program the microscope to perform automated fluorescence imaging. J.Z. created the Python code to analyze cell cycle phases of fluorescence images. M.D.S., M.P., J.Z., S.G., M.M., J.U.L., F.A., E.C., and A.E. supervised the experiments and contributed to manuscript preparation. E.T., A.E. and F.S.P. co-wrote the initial manuscript. All authors discussed the results and provided feedback on the manuscript.

Competing interests

The authors declare no competing interests.

Acknowledgements

This work was supported by the European Research Council (ERC) Starting Grant No. 852560 to F.S.P. and by the Italian Ministry of Education, University, and Research (MIUR) (FARE2020, Grant No. R20ZE54CTK) to F.S.P.

Data availability

All data that support the findings of this study are included within the article (and any supplementary files).

673 **Bibliography**

674 1. Harrer, S., Shah, P., Antony, B. & Hu, J. Artificial Intelligence for Clinical Trial Design. *Trends in*
675 *Pharmacological Sciences* **40**, 577–591 (2019).
676 2. Moor, M. *et al.* Foundation models for generalist medical artificial intelligence. *Nature* **616**, 259–
677 265 (2023).
678 3. Caudai, C. *et al.* AI applications in functional genomics. *Comput Struct Biotechnol J* **19**, 5762–
679 5790 (2021).
680 4. Ringel, M. S., Scannell, J. W., Baedeker, M. & Schulze, U. Breaking Eroom's law. *Nat Rev Drug*
681 *Discov* **19**, 833–834 (2020).
682 5. Scannell, J. W., Blanckley, A., Boldon, H. & Warrington, B. Diagnosing the decline in
683 pharmaceutical R&D efficiency. *Nature Reviews Drug Discovery* **11**, 191–200 (2012).
684 6. Esch, E. W., Bahinski, A. & Huh, D. Organs-on-chips at the frontiers of drug discovery. *Nature*
685 *Reviews Drug Discovery* **14**, 248–260 (2015).
686 7. Kapałczyńska, M. *et al.* 2D and 3D cell cultures - a comparison of different types of cancer cell
687 cultures. *Arch Med Sci* **14**, 910–919 (2018).
688 8. Fang, Y. & Eglen, R. M. Three-Dimensional Cell Cultures in Drug Discovery and Development.
689 *SLAS Discovery* **22**, 456–472 (2017).
690 9. Sonia Youhanna *et al.* Organotypic and Microphysiological Human Tissue Models for Drug
691 Discovery and Development—Current State-of-the-Art and Future Perspectives. *Pharmacol Rev*
692 **74**, 141 (2022).
693 10. Decoene, I. *et al.* Robotics-Driven Manufacturing of Cartilaginous Microtissues for Skeletal Tissue
694 Engineering Applications. *Stem Cells Translational Medicine* szad091 (2024)
695 doi:10.1093/stcltm/szad091.

696 11. Lee, S.-Y., Hwang, H. J. & Lee, D. W. Optimization of 3D-aggregated spheroid model (3D-ASM)
697 for selecting high efficacy drugs. *Sci Rep* **12**, 18937 (2022).
698 12. Nikolaev, M. *et al.* Homeostatic mini-intestines through scaffold-guided organoid morphogenesis.
699 *Nature* **585**, 574–578 (2020).
700 13. Quintard, C. *et al.* A microfluidic platform integrating functional vascularized organoids-on-chip.
701 *Nature Communications* **15**, 1452 (2024).
702 14. Rodoplu, D., Matahum, J. S. & Hsu, C.-H. A microfluidic hanging drop-based spheroid co-culture
703 platform for probing tumor angiogenesis. *Lab Chip* **22**, 1275–1285 (2022).
704 15. Skardal, A. *et al.* Multi-tissue interactions in an integrated three-tissue organ-on-a-chip platform.
705 *Sci Rep* **7**, 8837 (2017).
706 16. Lin, S., Schorpp, K., Rothenaigner, I. & Hadian, K. Image-based high-content screening in drug
707 discovery. *Drug Discovery Today* **25**, 1348–1361 (2020).
708 17. Kamiloglu, S., Sari, G., Ozdal, T. & Capanoglu, E. Guidelines for cell viability assays. *Food*
709 *Frontiers* **1**, 332–349 (2020).
710 18. Caliari, S. R. & Burdick, J. A. A practical guide to hydrogels for cell culture. *Nature Methods* **13**,
711 405–414 (2016).
712 19. Trask, O. J. Guidelines for Microplate Selection in High Content Imaging. *Methods Mol Biol* **1683**,
713 75–88 (2018).
714 20. Brooks, E. A., Jansen, L. E., Gencoglu, M. F., Yurkevicz, A. M. & Peyton, S. R. Complementary,
715 Semiautomated Methods for Creating Multidimensional PEG-Based Biomaterials. *ACS Biomater.*
716 *Sci. Eng.* **4**, 707–718 (2018).
717 21. Machillot, P. *et al.* Automated Buildup of Biomimetic Films in Cell Culture Microplates for High-
718 Throughput Screening of Cellular Behaviors. *Advanced Materials* **30**, 1801097 (2018).

22. Buxboim, A., Rajagopal, K., Brown, A. E. X. & Discher, D. E. How deeply cells feel: methods for thin gels. *Journal of Physics: Condensed Matter* **22**, 194116 (2010).
23. Atma, Y. Synthesis and Application of Fish Gelatin for Hydrogels/Composite Hydrogels: A Review. *BIOINTERFACE RESEARCH IN APPLIED CHEMISTRY* **12**, 3966–3976 (2022).
24. M. Di Sante *et al.* CALIPERS: Cell cycle-aware live imaging for phenotyping experiments and regeneration studies. *bioRxiv* 2024.12.19.629259 (2024) doi:10.1101/2024.12.19.629259.
25. McCain, M. L., Agarwal, A., Nesmith, H. W., Nesmith, A. P. & Parker, K. K. Micromolded gelatin hydrogels for extended culture of engineered cardiac tissues. *Biomaterials* **35**, 5462–5471 (2014).
26. Jensen, J. H. *et al.* Large-scale spontaneous self-organization and maturation of skeletal muscle tissues on ultra-compliant gelatin hydrogel substrates. *Scientific Reports* **10**, 13305 (2020).
27. Haug, I. J., Draget, K. I. & Smidsrød, O. Physical and rheological properties of fish gelatin compared to mammalian gelatin. *Food Hydrocolloids* **18**, 203–213 (2004).
28. Kim, Y.-J. & Uyama, H. Biocompatible Hydrogel Formation of Gelatin from Cold Water Fish via Enzymatic Networking. *Polymer Journal* **39**, 1040–1046 (2007).
29. Viscous liquids need special pipetting techniques. Viscous Liquids Need Special Pipetting Techniques - Eppendorf Italia Available at: https://www.eppendorf.com/it-it/lab-academy/life-science/cell-biology/viscous-liquids-need-special-pipetting-techniques/. (Accessed: 14th May 2025)
30. Lu, A., Zhu, J., Zhang, G. & Sun, G. Gelatin nanofibers fabricated by extruding immiscible polymer solution blend and their application in tissue engineering. *J. Mater. Chem.* **21**, 18674–18680 (2011).
31. Sancakli, A., Basaran, B., Arican, F. & Polat, O. Effects of bovine gelatin viscosity on gelatin-based edible film mechanical, physical and morphological properties. *SN Applied Sciences* **3**, 8 (2021).

742 32. Song, K., Ren, B., Zhai, Y., Chai, W. & Huang, Y. Effects of transglutaminase cross-linking process
743 on printability of gelatin microgel-gelatin solution composite bioink. *Biofabrication* **14**, (2021).
744 33. Bode, F., da Silva, M. A., Drake, A. F., Ross-Murphy, S. B. & Dreiss, C. A. Enzymatically Cross-
745 Linked Tilapia Gelatin Hydrogels: Physical, Chemical, and Hybrid Networks. *Biomacromolecules*
746 **12**, 3741–3752 (2011).
747 34. Sui, Y., Ding, H. & Spelt, P. D. M. Numerical Simulations of Flows with Moving Contact Lines.
748 *Annual Review of Fluid Mechanics* **46**, 97–119 (2014).
749 35. Hokeness, K. *et al.* IFN-gamma enhances paclitaxel-induced apoptosis that is modulated by
750 activation of caspases 8 and 3 with a concomitant down regulation of the AKT survival pathway in
751 cultured human keratinocytes. *Oncol Rep* **13**, 965–969 (2005).
752 36. Kim, H.-E., Cho, H., Ishihara, A., Kim, B. & Kim, O. Cell proliferation and migration mechanism
753 of caffeoylserotonin and serotonin via serotonin 2B receptor in human keratinocyte HaCaT cells.
754 *BMB Rep* **51**, 188–193 (2018).
755 37. Gustafsson, M. & Sebesta, M. Refractometry of microscopic objects with digital holography. *Appl.*
756 *Opt.* **43**, 4796–4801 (2004).
757 38. Hellesvik, M., Øye, H. & Aksnes, H. Exploiting the potential of commercial digital holographic
758 microscopy by combining it with 3D matrix cell culture assays. *Scientific Reports* **10**, 14680
759 (2020).
760 39. Cooper GM. The Eukaryotic Cell Cycle. in *The Cell: A Molecular Approach* (Sunderland (MA):
761 Sinauer Associates, 2000).
762 40. Sharma, N., Kosan, Z., Stallworth, J., Berbari, N. & Yoder, B. Soluble levels of cytosolic tubulin
763 regulate ciliary length control. *Molecular biology of the cell* **22**, 806–16 (2011).
764 41. Goler-Baron, V. & Assaraf, Y. G. Structure and Function of ABCG2-Rich Extracellular Vesicles
765 Mediating Multidrug Resistance. *PLOS ONE* **6**, e16007 (2011).

42. Elfarnawany, A. & Dehghani, F. Time- and Concentration-Dependent Adverse Effects of Paclitaxel on Non-Neuronal Cells in Rat Primary Dorsal Root Ganglia. *Toxics* **11**, (2023).

43. Seal, S. *et al.* A Decade in a Systematic Review: The Evolution and Impact of Cell Painting. Preprint at (2024).

44. Schindelin, J. *et al.* Fiji: an open-source platform for biological-image analysis. *Nature Methods* **9**, 676–682 (2012).

45. Schmidt, U., Weigert, M., Broaddus, C. & Myers, G. Cell Detection with Star-Convex Polygons. in *Medical Image Computing and Computer Assisted Intervention – MICCAI 2018* (eds. Frangi, A. F., Schnabel, J. A., Davatzikos, C., Alberola-López, C. & Fichtinger, G.) 265–273 (Springer International Publishing, Cham, 2018).

46. Phawaphuthanon, N., Yu, D., Ngamnikom, P., Shin, I.-S. & Chung, D. Effect of fish gelatine-sodium alginate interactions on foam formation and stability. *Food Hydrocolloids* **88**, 119–126 (2019).

47. Gao, L. *et al.* A Photopolymerizable Biocompatible Hyaluronic Acid Hydrogel Promotes Early Articular Cartilage Repair in a Minipig Model In Vivo. *Advanced Healthcare Materials* **12**, 2300931 (2023).

48. Agarwal, A. *et al.* Micropatterning Alginate Substrates for In Vitro Cardiovascular Muscle on a Chip. *Advanced Functional Materials* **23**, 3738–3746 (2013).

49. Yoon, H. *et al.* Cold Water Fish Gelatin Methacryloyl Hydrogel for Tissue Engineering Application. *PLOS ONE* **11**, e0163902 (2016).

50. Beaulieu, I., Geissler, M. & Mauzeroll, J. Oxygen Plasma Treatment of Polystyrene and Zeonor: Substrates for Adhesion of Patterned Cells. *Langmuir* **25**, 7169–7176 (2009).

51. NIS-Element. *NIS-Element software* https://www.nikoninstruments.com/Products/Software.

52. Coll, B. & Morel, J.-M. Non-Local Means Denoising. *Image Processing On Line* **1**, (2011).

53. J. Darbon, A. Cunha, T. F. Chan, S. Osher, & G. J. Jensen. Fast nonlocal filtering applied to electron cryomicroscopy. in *2008 5th IEEE International Symposium on Biomedical Imaging: From Nano to Macro* 1331–1334 (2008). doi:10.1109/ISBI.2008.4541250.

54. Tinevez, J.-Y. *et al.* TrackMate: An open and extensible platform for single-particle tracking. *Methods* **115**, 80–90 (2017).

55. Leo Guignard. LineageTree. https://github.com/GuignardLab/LineageTree.

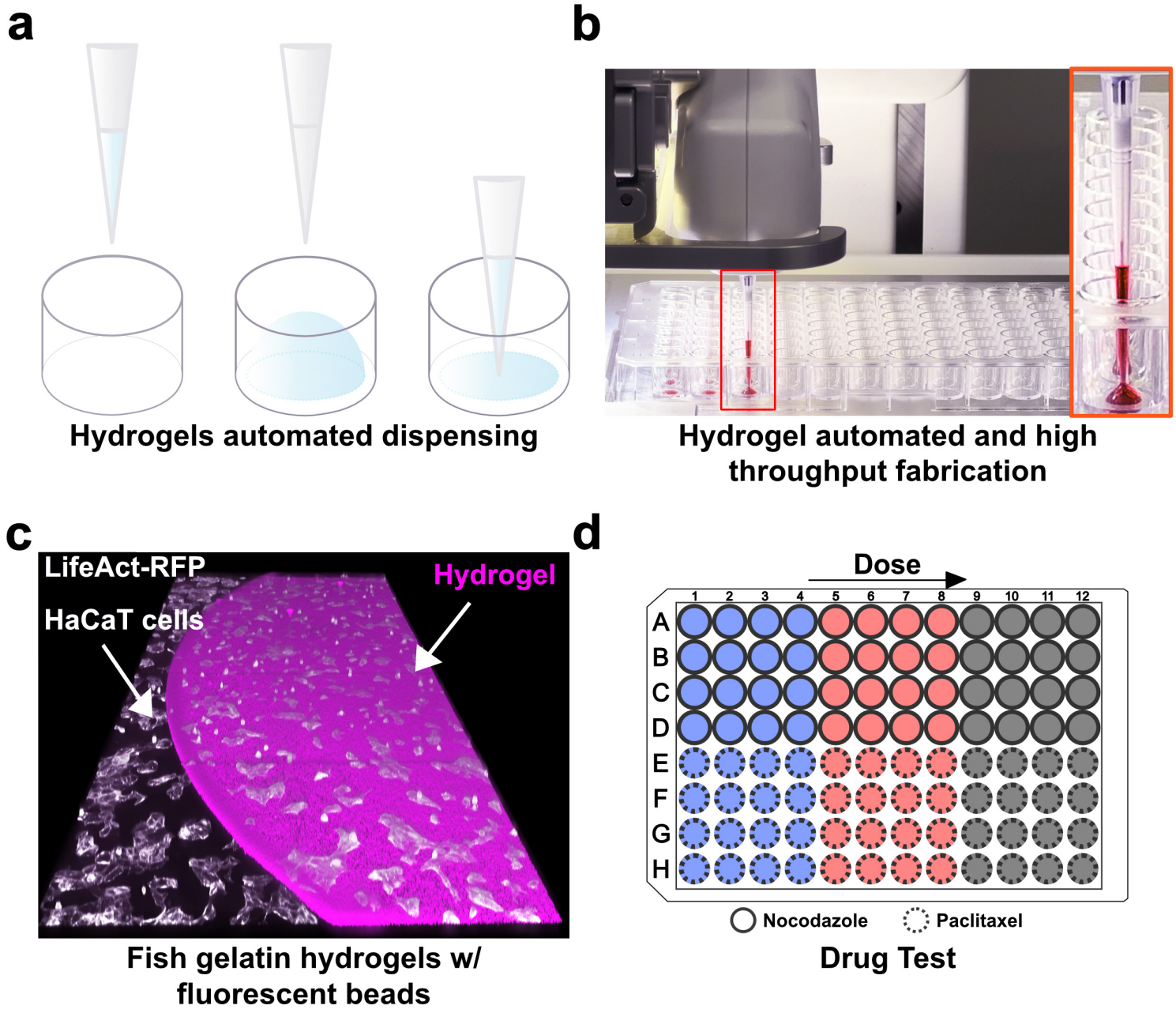
a
Hydrogels automated dispensing
b
Hydrogel automated and high throughput fabrication
c
LifeAct-RFP
HaCaT cells
Hydrogel
Fish gelatin hydrogels w/ fluorescent beads
d
Dose
1 2 3 4 5 6 7 8 9 10 11 12
A B C D E F G H
Nocodazole
Paclitaxel
Drug Test

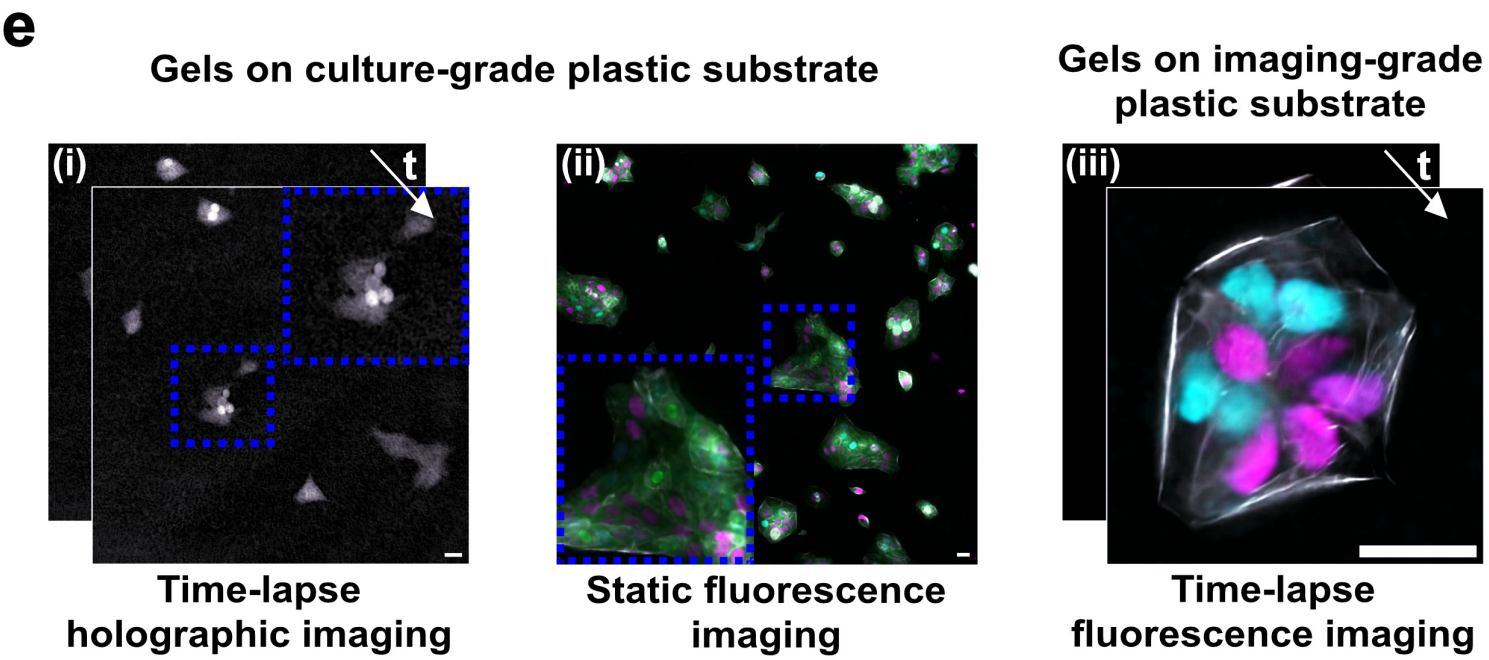
e
Gels on culture-grade plastic substrate
Gels on imaging-grade plastic substrate
(i)
t
(ii)
(iii)
t
Time-lapse holographic imaging
Static fluorescence imaging
Time-lapse fluorescence imaging

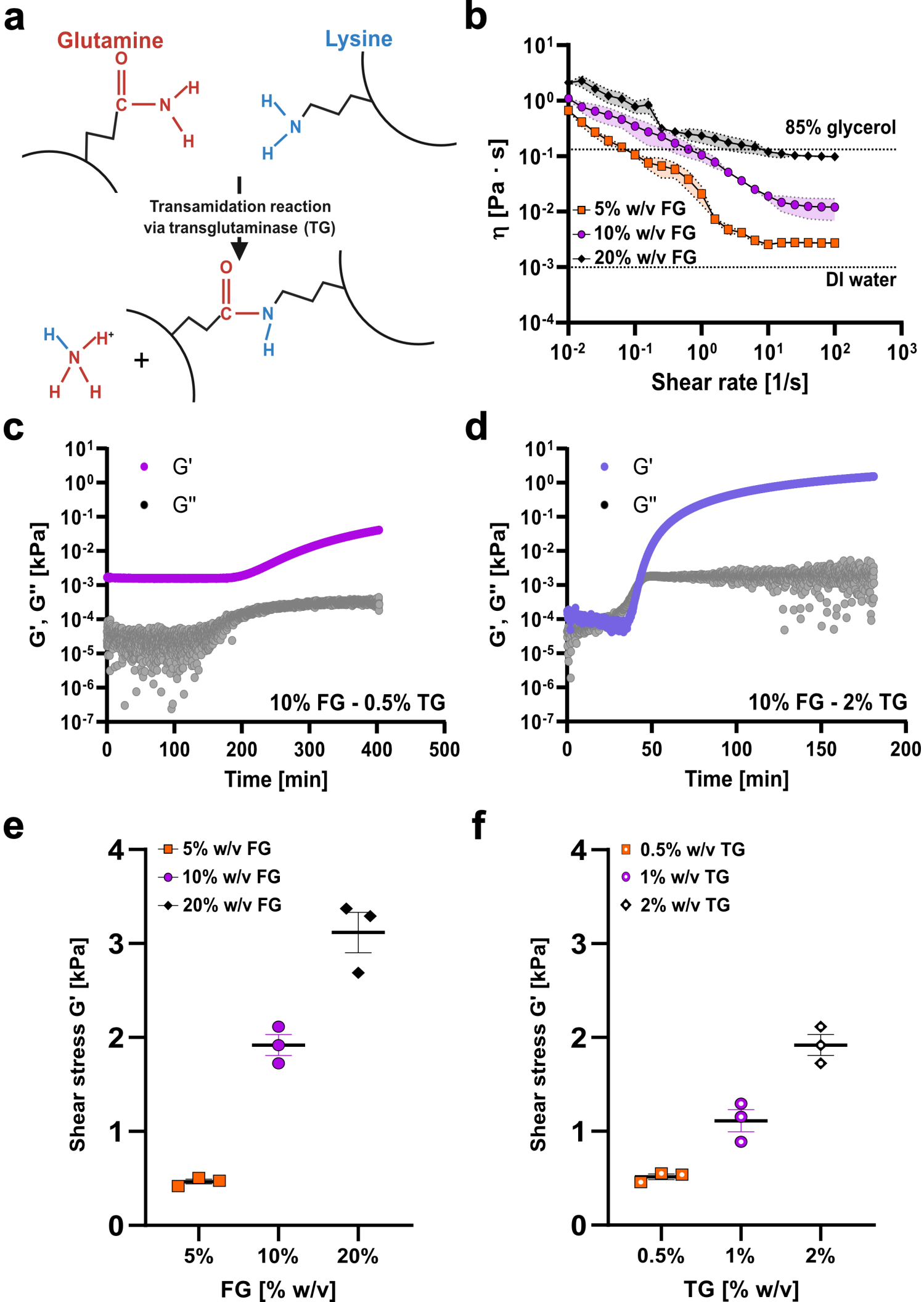
a
Glutamine
Lysine
Transamidation reaction
via transglutaminase (TG)
b
85% glycerol
5% w/v FG
10% w/v FG
20% w/v FG
DI water
η [Pa · s]
Shear rate [1/s]
c
G'
G''
G', G'' [kPa]
10% FG - 0.5% TG
Time [min]
d
G'
G''
G', G'' [kPa]
10% FG - 2% TG
Time [min]
e
5% w/v FG
10% w/v FG
20% w/v FG
Shear stress G' [kPa]
5%
10%
20%
FG [% w/v]
f
0.5% w/v TG
1% w/v TG
2% w/v TG
Shear stress G' [kPa]
0.5%
1%
2%
TG [% w/v]

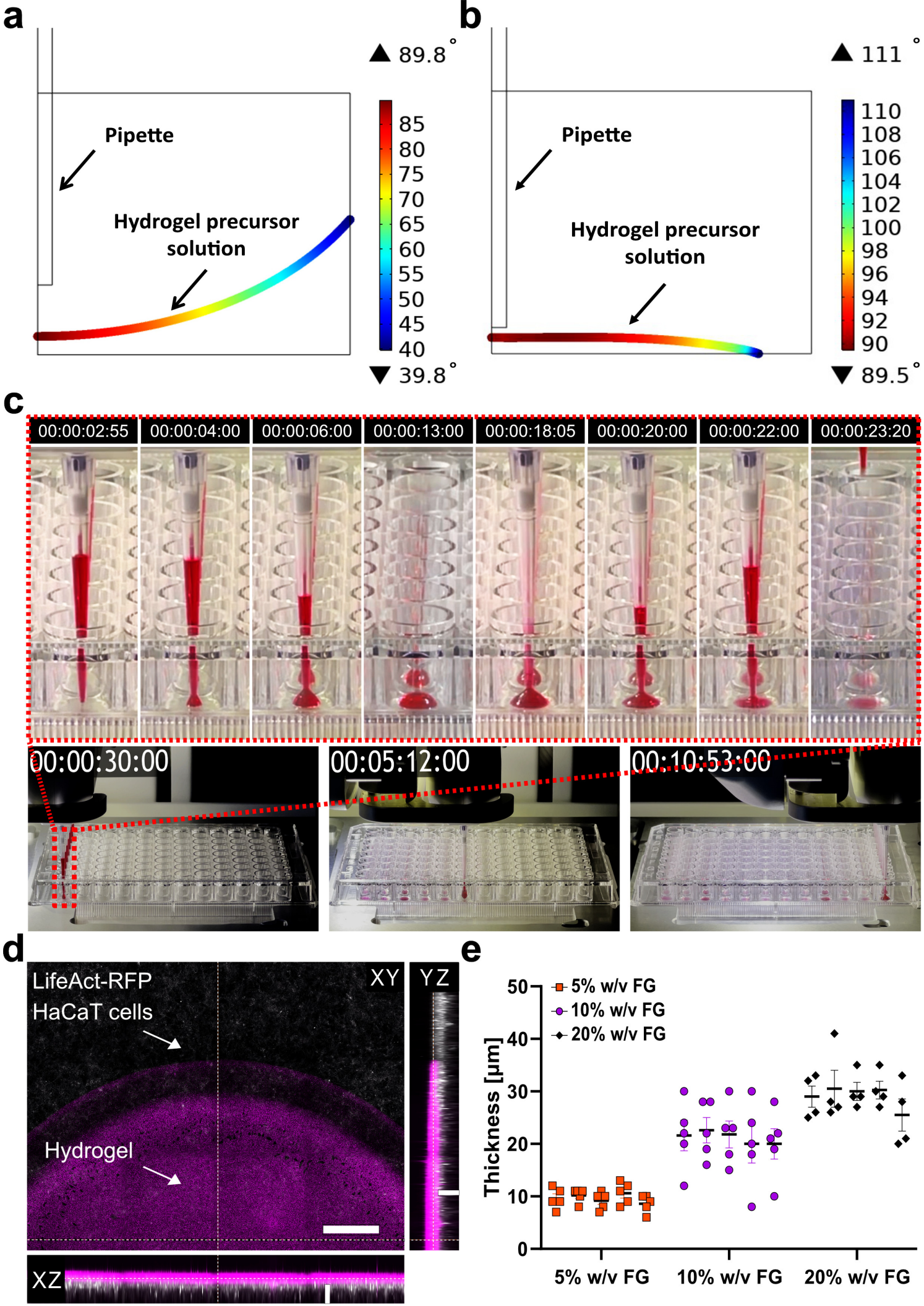
a
▲ 89.8°
Pipette
Hydrogel precursor solution
85
80
75
70
65
60
55
50
45
40
▼ 39.8°
b
▲ 111°
Pipette
Hydrogel precursor solution
110
108
106
104
102
100
98
96
94
92
90
▼ 89.5°
c
00:00:02:55
00:00:04:00
00:00:06:00
00:00:13:00
00:00:18:05
00:00:20:00
00:00:22:00
00:00:23:20
00:00:30:00
00:05:12:00
00:10:53:00
d
LifeAct-RFP
HaCaT cells
Hydrogel
XY
YZ
XZ
e
5% w/v FG
10% w/v FG
20% w/v FG
Thickness [µm]
0
10
20
30
40
50
5% w/v FG
10% w/v FG
20% w/v FG

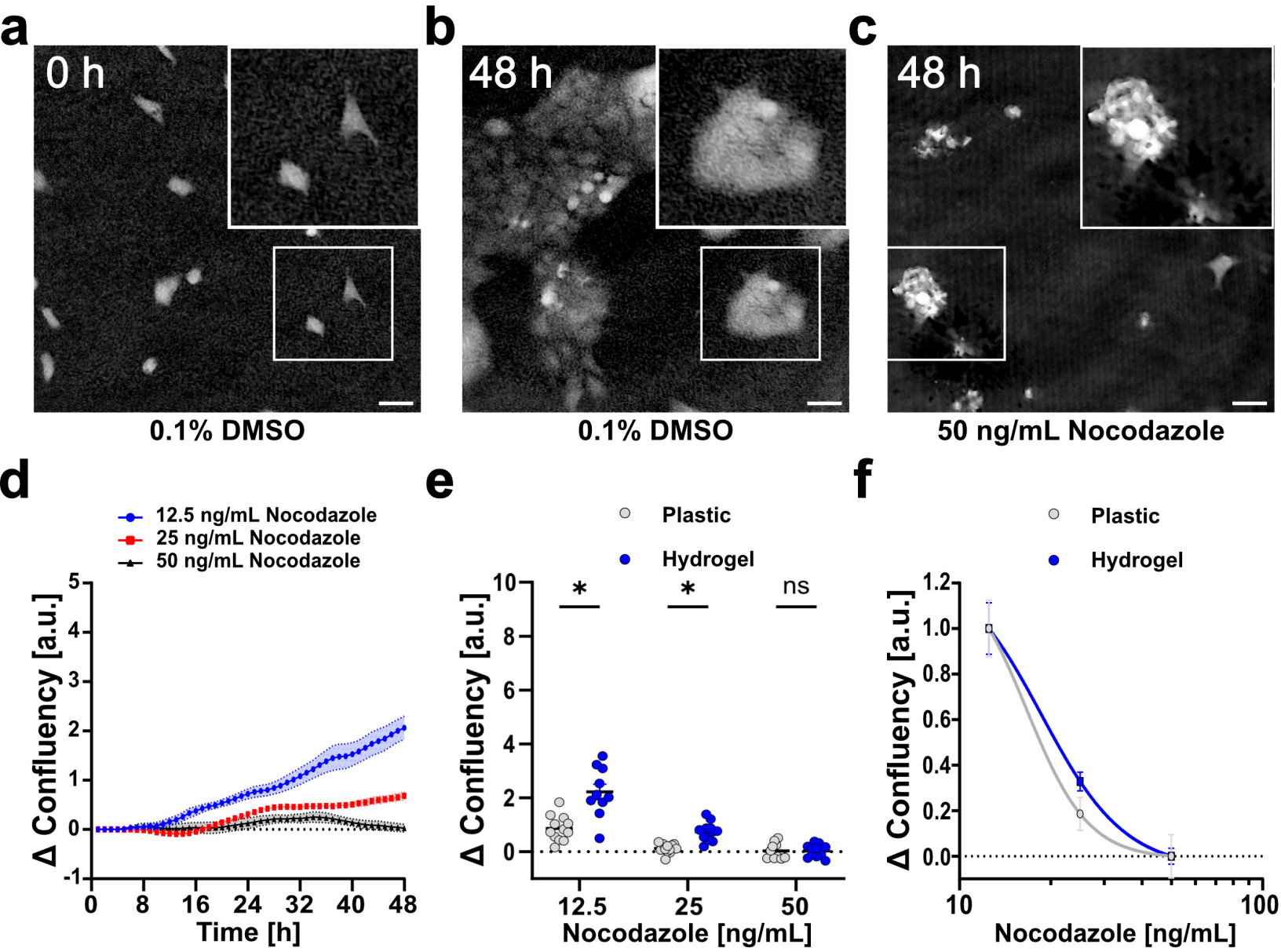
a
0 h
0.1% DMSO
b
48 h
0.1% DMSO
c
48 h
50 ng/mL Nocodazole
d
12.5 ng/mL Nocodazole
25 ng/mL Nocodazole
50 ng/mL Nocodazole
Δ Confluency [a.u.]
Time [h]
e
Plastic
Hydrogel
*
*
ns
Δ Confluency [a.u.]
Nocodazole [ng/mL]
f
Plastic
Hydrogel
Δ Confluency [a.u.]
Nocodazole [ng/mL]

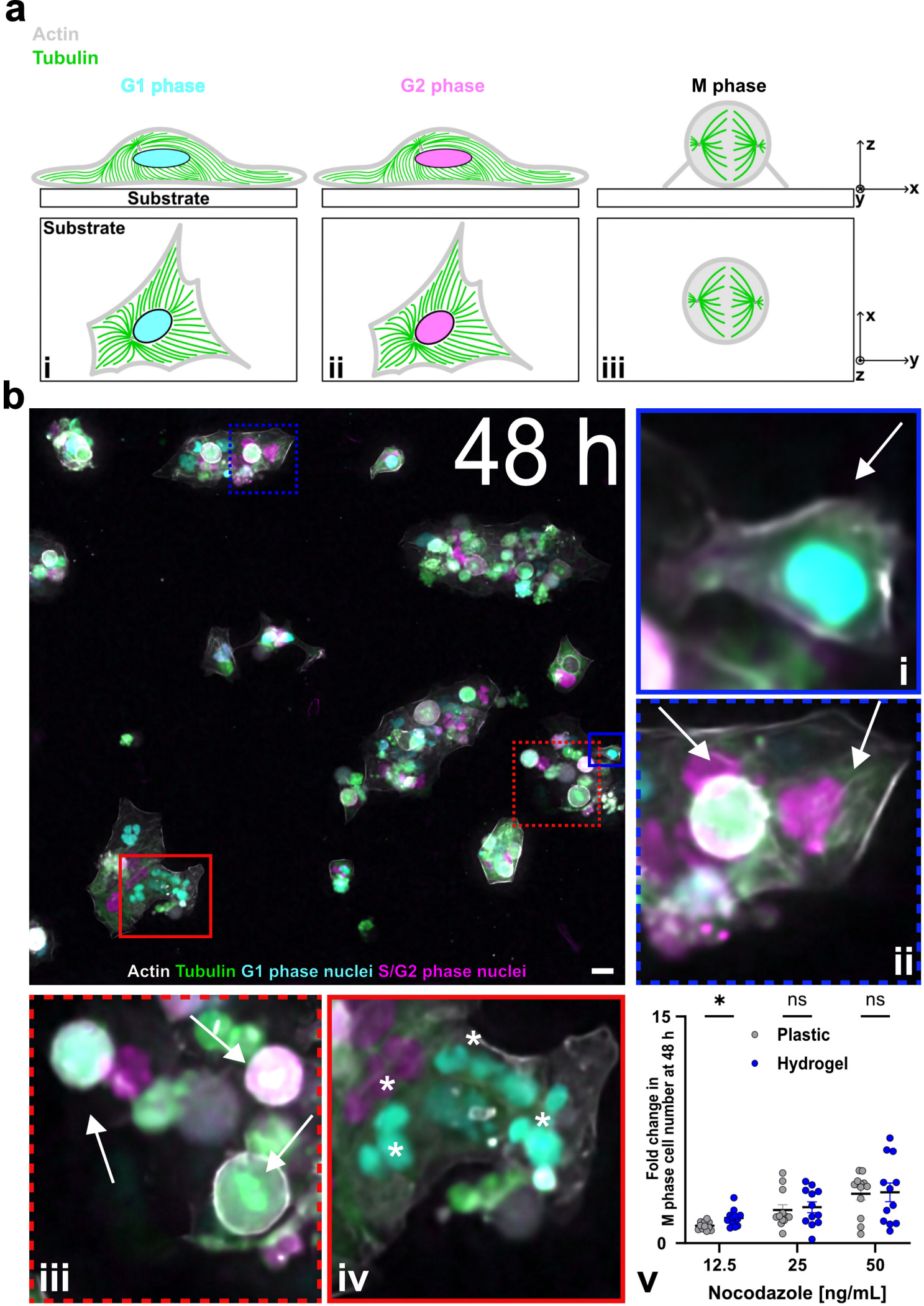
a
Actin
Tubulin
G1 phase
G2 phase
M phase
Substrate
Substrate
i
ii
iii
z
x
y
b
48 h
Actin Tubulin G1 phase nuclei S/G2 phase nuclei
i
ii
iii
iv
v
*
ns
ns
Plastic
Hydrogel
Fold change in M phase cell number at 48 h
15
0
12.5
25
50
Nocodazole [ng/mL]

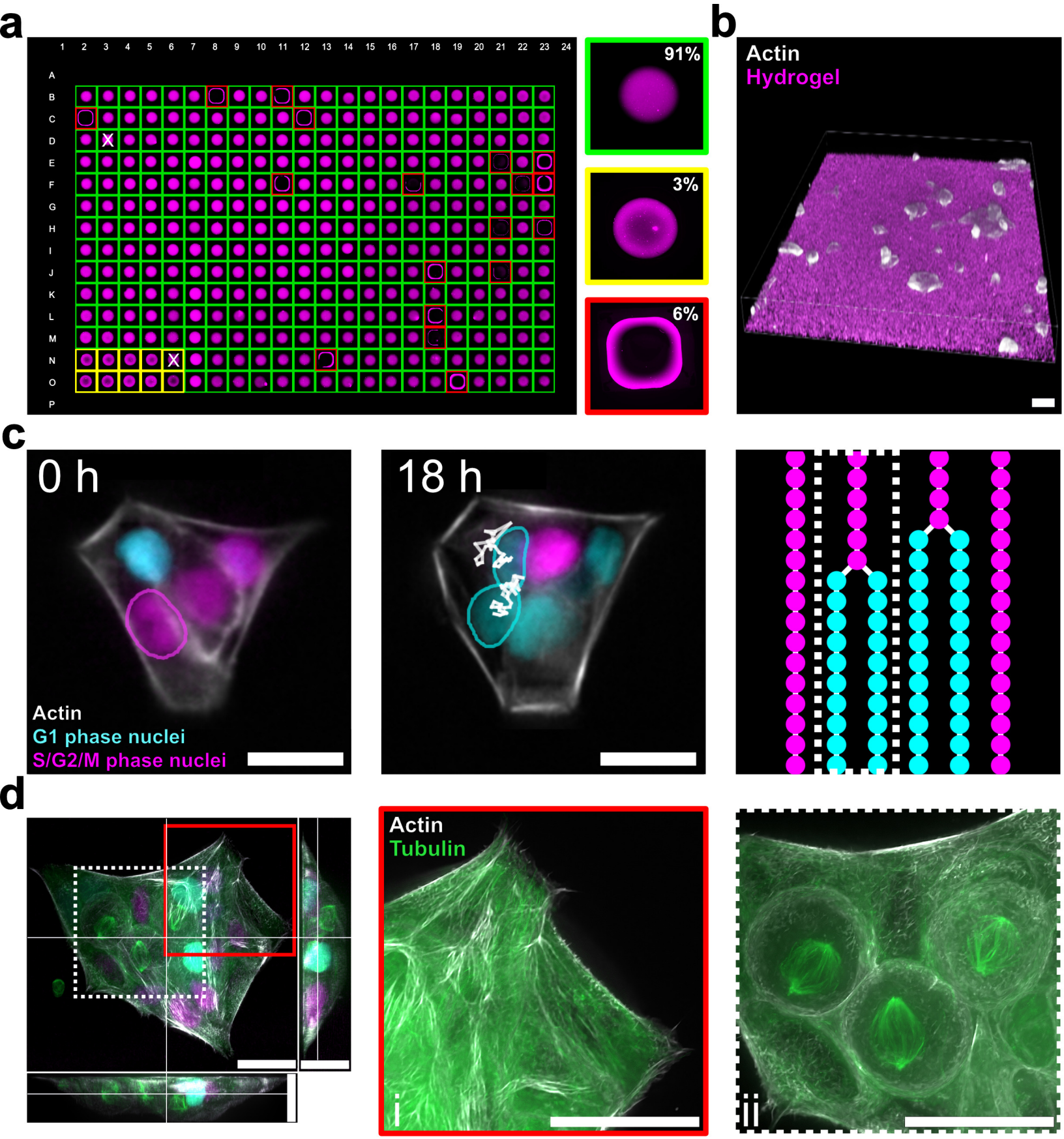
a
1 2 3 4 5 6 7 8 9 10 11 12 13 14 15 16 17 18 19 20 21 22 23 24
A B C D E F G H I J K L M N O P
91%
3%
6%
b
Actin
Hydrogel
c
0 h
18 h
Actin
G1 phase nuclei
S/G2/M phase nuclei
d
Actin
Tubulin
i
ii